

## Original Article

**Cite this article:** Pang Z, Gao F, Du Y, Du Y, Zong Z, Xie J, and Xin F (2020) Late Jurassic to Early Cretaceous magmatism in the Xiong'er-shan gold district, central China: implications for gold mineralization and geodynamics. *Geological Magazine* **157**: 435–457. <https://doi.org/10.1017/S0016756819000888>

Received: 2 January 2019

Revised: 14 June 2019

Accepted: 8 July 2019

First published online: 9 October 2019


**Keywords:**

Late Jurassic to Early Cretaceous magmatism; petrogenesis; gold mineralization; tectonic evolution; Xiong'er-shan area

**Author for correspondence:**

Fuping Gao, Email: [gfp2000@163.com](mailto:gfp2000@163.com)

# Late Jurassic to Early Cretaceous magmatism in the Xiong'er-shan gold district, central China: implications for gold mineralization and geodynamics

Zhenshan Pang<sup>1</sup>, Fuping Gao<sup>2</sup> , Yangsong Du<sup>2</sup>, Yilun Du<sup>1</sup>, Zhaojian Zong<sup>2</sup>, Jinsong Xie<sup>3</sup> and Fengpei Xin<sup>3</sup>

<sup>1</sup>Development and Research Center of China Geological Survey, Beijing 100037, P.R. China; <sup>2</sup>School of the Earth Sciences and Resources, China University of Geosciences, Beijing 100083, P.R. China and <sup>3</sup>No. 1 Institute of Geological and Mineral Resources Survey of Henan, Luoyang 471023, P.R. China

**Abstract**

The Xiong'er-shan area is the third largest gold-producing district in China. The Late Jurassic to Early Cretaceous magmatism in the Xiong'er-shan area can be divided into two episodes: early (165–150 Ma) and late (138–113 Ma). Laser ablation – inductively coupled plasma – mass spectrometry (LA-ICP-MS) zircon U–Pb dating yields ages of  $160.7 \pm 0.6$  Ma and  $127.2 \pm 1.0$  Ma for the Wuzhangshan and Huashan monzogranites in the Xiong'er-shan area, respectively, representing the two magmatic episodes. The Wuzhangshan monzogranites exhibit adakite-like geochemical features (e.g. high Sr/Y ratios, low Yb and Y contents). Their Sr–Nd–Hf isotopic compositions are consistent with those of the amphibolites of the Taihua Group, indicating that the Wuzhangshan monzogranites were formed from partial melting of the Taihua Group metamorphic rocks. Compared to the Wuzhangshan rocks, the Huashan monzogranites have higher MgO, Cr, Co and Ni contents, but lower Sr/Y and  $Fe^{3+}/Fe^{2+}$ . All the samples from the Huashan monzogranites plot in the area between the Taihua Group amphibolite rocks and the mantle rocks in the  $(^{87}Sr/^{86}Sr)_t$  vs  $\epsilon Nd(t)$  and age vs  $\epsilon Hf(t)$  diagrams, suggesting that the Huashan monzogranites were probably generated by mixing of mantle-derived magmas and the Taihua Group metamorphic basement melts. The gold mineralization (136–110 Ma) is coeval with the emplacement of the late-episode magmas, implying that crustal–mantle mixed magma might be a better target for gold mineralization compared to the ancient metamorphic basement melt. The data presented in this study further indicate that the transformation of the lithosphere from thickening to thinning in the Xiong'er-shan area probably occurred between ~160 Ma and ~127 Ma, and that the gold mineralization in this area was probably related to lithospheric thinning.

**1. Introduction**

Although magmas in intracontinental environments represent a volumetrically minor component of the global magmatic budget (Kuritani *et al.* 2009), they are of considerable geologic interest and have attracted considerable attention (e.g. Gao *et al.* 2004; Van der Meer *et al.* 2017; and references therein), because of their critical geochemical features that distinguish them from 'normal' mid-ocean ridge and arc magmas, but also because they are associated with many world-class ore deposits (e.g. Cr, Ni, Mo and Au deposits, Naldrett, 1999, 2004; Pirajno *et al.* 2004). Intracontinental magmatism occurring in different tectonic settings has been attributed to several possible processes, such as deep mantle plumes, back-arc spreading, continental rifting, stagnant slab, and lithospheric thinning (e.g. Gao *et al.* 2004, 2014; Kuritani *et al.* 2009, 2017; Zhao *et al.* 2012; Van der Meer *et al.* 2017). This suggests that the origins of intracontinental magmatism require detailed investigations in each individual setting (Kuritani *et al.* 2009).

The Qinling orogenic belt (QOB), suturing the North China Craton (NCC) to the north and the Yangtze Craton to the south (Fig. 1a, b), is an important collisional orogen in eastern Asia (Zhang *et al.* 1996; Mao *et al.* 2002). The final collision between the Yangtze and North China cratons occurred between 250 and 210 Ma (e.g. Ratschbacher *et al.* 2003; Dong & Santosh, 2016; Tang *et al.* 2019; and references therein), and then the tectonic regime of the QOB transformed into a post-collisional extensional environment between 210 and 200 Ma (e.g. Dong & Santosh, 2016; Tang *et al.* 2019). This was accompanied by distinct pulses of Triassic magmatism in volcanic arc, syn-collisional and post-collisional settings (e.g. Dong & Santosh, 2016; Tang *et al.* 2019). In addition to the Triassic magmatism, the southern margin of the NCC in the QOB also records intensive intracontinental tectonic–magmatic activity during the Late Jurassic to Early Cretaceous, with widely exposed igneous rocks (e.g. Mao *et al.* 2010;

Zhao *et al.* 2012; Gao *et al.* 2014; Gao & Zhao, 2017) and many world-class Mo–Au–Ag–Pb–Zn ore deposits (e.g. Mao *et al.* 2002, 2011; Chen *et al.* 2008; Tang *et al.* 2013; Tang, 2014; Bao *et al.* 2017; Tian *et al.* 2017). It has been generally considered that the generation of the Late Jurassic to Early Cretaceous magmatism in the southern margin of the NCC is controlled by intraplate processes – craton destruction (the process of decratonization) and lithospheric thinning – triggered by the far-field effect of the subduction of the Palaeo-Pacific Plate beneath the NCC (e.g. Lapiere *et al.* 1997; Mao *et al.* 2002, 2010, 2011; Ratschbacher *et al.* 2003; Windley *et al.* 2010). Therefore, the Late Jurassic to Early Cretaceous magmas in the southern margin of the NCC along the QOB are of considerable geologic interest, not only because they are associated with one of the most important gold polymetallic metallogenic belts in China, but also because of their geodynamic context and likely relationship to craton destruction (Zhao *et al.* 2012).

Late Jurassic to Early Cretaceous granites along the southern margin of the NCC have been extensively studied in the past decades, but there is still considerable uncertainty about key issues related to these magmatic rocks, such as (1) the petrogenesis of these rocks: these granites have been proposed to be derived from partial melting of ancient crystalline basement of the NCC, which mixed with mantle-derived melts (e.g. Li *et al.* 2012; Gao *et al.* 2014; Gao & Zhao, 2017), or from the subducted continental crust of the northern margin of the Yangtze Craton (e.g. Bao *et al.* 2014, 2017); (2) the link between the magmatism and gold: some researchers suggest that gold mineralization has resulted from Late Jurassic to Early Cretaceous magmatic–hydrothermal processes (e.g. Yao *et al.* 2009; Tang *et al.* 2013; Tian *et al.* 2017), but other researchers classified these gold deposits as orogenic type (e.g. Goldfarb *et al.* 1998; Mao *et al.* 2002; Chen *et al.* 2008) or greenstone type (e.g. Li *et al.* 1996), assigning the metamorphic rocks as the main source for the metallic ores (e.g. Li *et al.* 1996; Li & Santosh, 2017); (3) the timing of lithospheric thinning: the age estimates for this event given by previous studies are variable, ranging from 159 Ma to 108 Ma (e.g. Gao *et al.* 2004; Mao *et al.* 2010; Li *et al.* 2012; Zhao *et al.* 2012). Recently, the Late Jurassic to Early Cretaceous intrusions in the southern margin of the NCC were recognized as the products of two magmatic stages: 160–135 Ma and 135–110 Ma (Mao *et al.* 2010; Gao & Zhao, 2017). The intrusions in these two stages show different chemical and isotopic compositions (Gao & Zhao, 2017), implying different magmatic sources in potentially distinct tectonic settings. Identification of the two magmatic intervals in the southern margin of the NCC is important for evaluating the geodynamics of this region and understanding the genesis of magmatic rocks and associated ore deposits.

The Xiong'er shan area, a representative region for the south margin of the NCC, QOB, exposes several Late Jurassic to Early Cretaceous granitic plutons and hosts numerous Au, Mo, Pb, Zn and Ag deposits (Fig. 1c), and ranks as the third largest gold concentration in China (Mao *et al.* 2002; Deng *et al.* 2014). The Wuzhangshan and Huashan plutons are the two largest batholiths in the Xiong'er shan area. New high-precision zircon U–Pb dates presented in this study indicate that the Wuzhangshan and Huashan monzogranites were emplaced at c. 160 Ma and 127 Ma, respectively, suggesting that they preserve the imprints of two magmatic episodes during the Late Jurassic to Early Cretaceous in the south margin of the NCC, respectively. Furthermore, we provide new petrographic observations, whole-rock major and trace element geochemistry, laser ablation – inductively coupled plasma – mass spectrometry (LA-ICP-MS) zircon U–Pb ages, and Sr–Nd–Hf isotopes for the

Wuzhangshan and Huashan monzogranites, to constrain their petrogenesis, geodynamics setting and relationship with gold deposits in the southern margin of the NCC.

## 2. Geological setting

The Qinling orogenic belt is bound by the Lingbao–Lushan–Wuyang fault with the NCC to the north, and the Mianlue suture zone with the Yangtze Craton to the south (Fig. 1b). The belt can be subdivided into three tectonic units from north to south (Zhang *et al.* 1996): the southern margin of the NCC, the North and South Qinling belts (Fig. 1b). The Luonan–Luanchuan regional fault separates the southern margin of the NCC and the North Qinling belt, whereas the North and South Qinling belts are separated by the Shangdan suture zone.

The Xiong'er shan area is located in the south margin of the North China Craton, QOB (Fig. 1b). Basement rocks of this region are Neoproterozoic to Palaeoproterozoic Taihua group (c. 2.84–2.26 Ga, Xu *et al.* 2009; Huang *et al.* 2012) that consist of biotite–plagioclase gneiss, plagioclase–amphibole gneiss and amphibolite, all belonging to tonalite–trondhjemite–granodiorite (TTG) suites (Huang *et al.* 2012). These rocks are discordantly overlain by the Mesoproterozoic Xiong'er group (c. 1.80–1.75 Ma, Zhao *et al.* 2004), a low-grade volcanic succession ranging from 3.0 to 7.6 km in thickness, covering an area of >6000 km<sup>2</sup> (Zhao *et al.* 2004). It consists mainly of basaltic andesite and andesite, with minor dacite and rhyolite (Zhao *et al.* 2004). These rocks are characterized by large-ion lithophile elements and light rare earth elements (LREE) enrichments and high-field-strength elements (HFSE) depletion, indicating hydrous melting of a mantle wedge in a subduction zone (He *et al.* 2010). The Xiong'er Group is discordantly overlain by Meso- to Neo-proterozoic littoral facies clastic–carbonate rocks and alkaline volcanic rocks of the Guandaokou and Luanchuan groups.

The Mesozoic magmatic rocks in the Xiong'er shan area mainly formed in two periods: Triassic and Late Jurassic to Early Cretaceous. The Triassic magmatic rocks sporadically occur in the Xiong'er shan area. The Late Jurassic to Early Cretaceous magmatic rocks are widespread in the Xiong'er shan area and occur as large batholiths (e.g. Huashan and Wuzhangshan) or small porphyritic bodies (e.g. Qiyugou, Lemengou and Banzhusi) (Fig. 1c). These rocks are composed of biotite amphibole granite, biotite granite, monzogranite and syenogranite (Gao *et al.* 2014; Nie *et al.* 2015).

## 3. Samples and analytical techniques

### 3.a. Sampling and petrography

Geochemical and zircon U–Pb dating samples were collected from the Wuzhangshan and Huashan batholiths. The Wuzhangshan pluton, covering an area of ~60 km<sup>2</sup> (Nie *et al.* 2015), intruded into metamorphic rocks of the Taihua Group in the north and volcanic rocks of the Xiong'er Group in the south (Fig. 1c). The rocks are generally reddish, medium- to coarse-grained porphyritic monzogranites (Fig. 2a, b; Fig. S1 in Supplementary Material available online at <https://doi.org/10.1017/S0016756819000888>), consisting of 3–6 % phenocrysts (mainly plagioclase, with lesser K-feldspar) in a medium-grained granular matrix of K-feldspar (25–30 %), plagioclase (30–35 %), quartz (20–25 %), amphibole (5–10 %) and minor biotite (Fig. 2c); accessory minerals include zircon, titanite, magnetite and apatite. Feldspars are mainly platy, up to 1.5 cm in diameter (Fig. 2a). Amphiboles are euhedral to subhedral

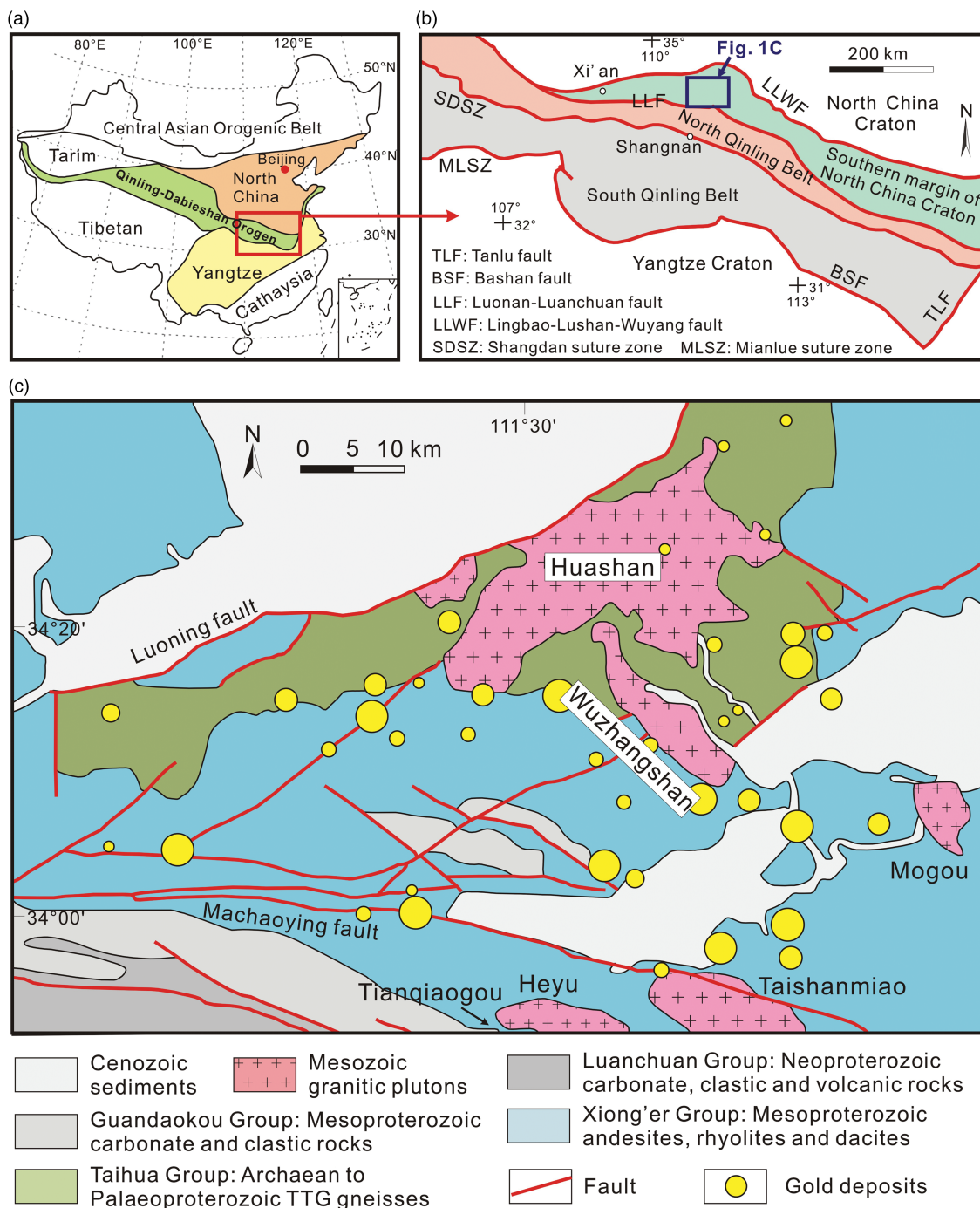


**Fig. 1.** (Colour online) (a) Simplified structural map of China showing the major tectonic subdivisions of China and the location of Qinling Orogenic Belt (modified from Tang *et al.* 2019). (b) Tectonic framework of the Qinling Orogenic Belt (modified after Zhang *et al.* 1996). (c) Geology and the distribution of the gold deposits in the Xiong'er shan area (modified after Tang *et al.* 2019).

(Fig. 2c) and exhibit no alteration, with a grain size of 0.2–2 mm. Quartz shows granular shape, with a grain size of 20–800 μm (Fig. 2b, c). The Wuzhangshan monzogranites contain sporadic xenoliths of the basement rocks, most of which are amphibolites of the Taihua Group, and have sharp boundaries.

The Huashan pluton intruded into the metamorphic rocks of the Taihua Group and covers an area of 300 km<sup>2</sup> (Nie *et al.* 2015). The pluton contains a small amount of mafic magmatic enclaves, which are ellipsoidal to spherical in shape, and have sharp or blurred boundaries with their host rocks (Nie *et al.* 2015). Rocks

from the Huashan pluton are mainly composed of medium- to fine-grained monzogranites and porphyritic monzogranites (Fig. S1 in Supplementary Material at <https://doi.org/10.1017/S0016756819000888>). The medium- to fine-grained monzogranites (Fig. 2d) are located at the north part of the pluton with an outcrop area of ~100 km<sup>2</sup>. They are light grey in colour and contain K-feldspar (25–30 %), plagioclase (30–35 %), quartz (20–25 %), biotite (5–8 %) and local amphibole (0–2 %), and accessory zircon, titanite, magnetite and apatite (Fig. 2e, f). The porphyritic monzogranites are located at the southern part of the pluton with an

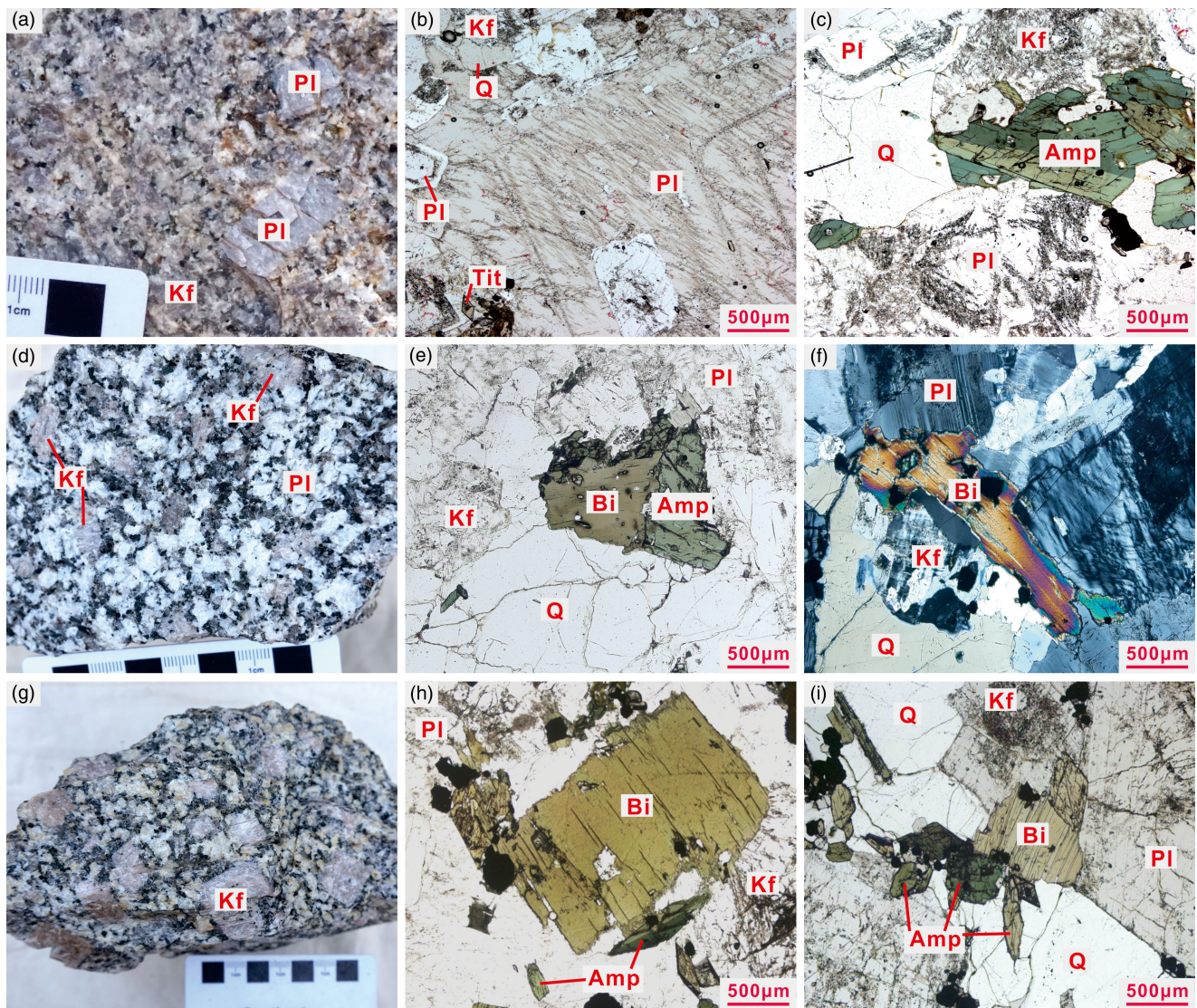


**Fig. 2.** (Colour online) Photographs of representative samples from the Wuzhangshan and Huashan monzogranites. (a, b) The Wuzhangshan monzogranites show porphyritic texture with euhedral phenocrysts of plagioclase. (c) The medium-grained granular matrix of the Wuzhangshan monzogranite, showing a mineral assemblage of K-feldspar + plagioclase + quartz + amphibole. (d) The medium- to fine-grained monzogranite of the Huashan pluton. (e, f) Photomicrographs of the Huashan medium- to fine-grained monzogranites, showing a mineral assemblage of K-feldspar + plagioclase + quartz + amphibole + biotite. (g) Porphyritic monzogranite of the Huashan pluton. (h, i) The medium-grained granular matrix of the Huashan porphyritic monzogranites, showing a mineral assemblage of K-feldspar + plagioclase + quartz + biotite + amphibole. Pl – plagioclase; Kf – K-feldspar; Q – quartz; Amp – amphibole; Bi – biotite; Tit – titanite.

outcrop area of ~200 km<sup>2</sup>. They are light grey to pink and show porphyritic textures. The phenocrysts are mainly K-feldspar with a grain size of 0.5–3 cm (Fig. 2g). The matrix displays medium- to fine-grained texture, consisting of K-feldspar (30–35 %), plagioclase (25–30 %), quartz (20–25 %), biotite (5–8 %) and local amphibole (1–3 %) (Fig. 2h, i). Accessory minerals include apatite, zircon, magnetite and titanite.

### 3.b. *In situ* zircon U–Pb dating and Hf isotopes

About 5 kg of each sample was crushed and sieved for separating zircon grains using standard magnetic and heavy liquid separation procedures. About 80–150 grains were mounted in epoxy and then polished to expose crystal mid-sections. Photographs in polarized and reflected light and cathodoluminescence (CL) images were prepared to examine the internal structures and to select points for analysis.

*In situ* zircon U–Pb dating was conducted using LA-ICP-MS at the Institute of Geology, Chinese Academy of Geological Sciences, Beijing, China, following the procedures in Hou *et al.* (2009). The ablation system operated at a wavelength of 193 nm using a spot diameter of ~32 μm. The data were calibrated according to the M127 reference zircon (U: 923 ppm; Th: 439 ppm; Th/U: 0.475, Nasdala *et al.* 2008). The zircon GJ-1 with an age of 599.8 ± 1.7 Ma (Jackson *et al.* 2004) and Plesovice with an age of 337.13 ± 0.37 Ma (Sláma *et al.* 2008) were used as reference standards. Data processing was conducted using the ICPMSDataCal programs. Common Pb corrections were made following methods of Anderson (2002). The analytical data are summarized in Table 1 and graphically presented on concordia diagrams with a 1σ error. The ages are weighted means with 2σ errors that were calculated using Isoplot 3.0 at 95 % confidence levels. LA-ICP-MS zircon U–Pb dating yields ages of 336.8 ± 1.0 Ma (*n* = 6) for

**Table 1.** LA-ICP-MS zircon U–Pb analyses for the Wuzhangshan and Huashan monzogranites in the Xiong'er shan area

Spots	Th/U	<sup>207</sup> Pb/ <sup>206</sup> Pb		<sup>207</sup> Pb/ <sup>235</sup> U		<sup>206</sup> Pb/ <sup>238</sup> U		<sup>207</sup> Pb/ <sup>206</sup> Pb		<sup>207</sup> Pb/ <sup>235</sup> U		<sup>206</sup> Pb/ <sup>238</sup> U	
		Ratio	1σ	Ratio	1σ	Ratio	1σ	Ma	1σ	Ma	1σ	Ma	1σ
<i>WZS03 monzogranite of the Wuzhangshan pluton</i>													
WZS03-1	0.29	0.05135	0.00120	0.17819	0.00383	0.02518	0.00019	257	35	167	3	160	1
WZS03-2	0.25	0.05477	0.00138	0.18971	0.00442	0.02513	0.00020	403	38	176	4	160	1
WZS03-3	0.24	0.06693	0.00176	0.23339	0.00567	0.02530	0.00022	836	36	213	5	161	1
WZS03-4	0.69	0.04996	0.00108	0.17378	0.00343	0.02524	0.00018	193	33	163	3	161	1
WZS03-5	0.99	0.05020	0.00925	0.17560	0.03192	0.02538	0.00080	204	311	164	28	162	5
WZS03-6	0.35	0.04995	0.00089	0.17500	0.00275	0.02542	0.00017	193	24	164	2	162	1
WZS03-7	0.68	0.04993	0.00266	0.17393	0.00897	0.02527	0.00032	192	96	163	8	161	2
WZS03-8	0.33	0.06191	0.00138	0.21460	0.00436	0.02515	0.00019	671	30	197	4	160	1
WZS03-9	0.27	0.07047	0.00147	0.24752	0.00463	0.02548	0.00019	942	26	225	4	162	1
WZS03-10	0.22	0.05378	0.00114	0.18640	0.00360	0.02514	0.00018	362	31	174	3	160	1
WZS03-11	0.44	0.05063	0.00272	0.17638	0.00920	0.02528	0.00031	224	98	165	8	161	2
WZS03-12	0.32	0.06402	0.00121	0.22185	0.00369	0.02514	0.00018	742	23	203	3	160	1
WZS03-13	0.24	0.04942	0.00153	0.17217	0.00503	0.02527	0.00022	168	52	161	4	161	1
WZS03-14	0.29	0.05089	0.00091	0.17684	0.00278	0.02521	0.00017	236	24	165	2	160	1
WZS03-15	0.28	0.05184	0.00124	0.18108	0.00399	0.02534	0.00019	278	37	169	3	161	1
WZS03-16	0.32	0.06755	0.00134	0.24210	0.00425	0.02600	0.00019	855	24	220	3	165	1
WZS03-17	0.36	0.05084	0.00121	0.17803	0.00391	0.02540	0.00019	234	37	166	3	162	1
WZS03-18	0.26	0.04944	0.00106	0.17241	0.00338	0.02530	0.00018	169	32	162	3	161	1
WZS03-19	0.24	0.05070	0.00131	0.17530	0.00432	0.02508	0.00019	227	61	164	4	160	1
<i>WZS03 inherited zircons</i>													
WZS03-LH01	0.37	0.12522	0.00297	4.32315	0.09416	0.25047	0.00268	2032	24	1698	18	1441	14
WZS03-LH02	0.36	0.16092	0.00169	10.2153	0.06856	0.46053	0.00281	2465	5	2454	6	2442	12
WZS03-LH03	0.48	0.11729	0.00272	1.10155	0.02394	0.06811	0.00055	1915	43	754	12	425	3
<i>HS09 monzogranite of the Huashan pluton</i>													
HS09-01	0.95	0.04906	0.00036	0.13806	0.00318	0.02040	0.00045	150	31	131	3	130	3
HS09-02	0.91	0.04898	0.00045	0.13523	0.00259	0.02002	0.00037	146	22	129	2	128	2
HS09-03	0.86	0.04950	0.00058	0.13594	0.00336	0.01991	0.00039	172	42	129	3	127	2
HS09-04	0.90	0.04864	0.00044	0.13064	0.00236	0.01948	0.00036	132	114	125	2	124	2
HS09-05	1.13	0.05036	0.00064	0.13947	0.00306	0.02010	0.00049	213	14	133	3	128	3
HS09-06	1.05	0.05178	0.00086	0.14204	0.00524	0.01985	0.00047	276	39	135	5	127	3
HS09-07	1.02	0.05486	0.00166	0.14975	0.00768	0.01970	0.00050	406	67	142	7	126	3
HS09-08	0.94	0.04925	0.00048	0.13922	0.00252	0.02051	0.00038	167	22	132	2	131	2
HS09-09	1.02	0.04839	0.00046	0.13293	0.00264	0.01992	0.00034	117	22	127	2	127	2
HS09-10	0.98	0.04928	0.00048	0.13494	0.00290	0.01985	0.00036	161	22	129	3	127	2
HS09-11	0.76	0.05396	0.00057	0.14410	0.00356	0.01936	0.00039	369	22	137	3	124	2
HS09-12	0.97	0.05033	0.00111	0.14162	0.00467	0.02038	0.00034	209	50	134	4	130	2
HS09-13	0.86	0.05266	0.00133	0.14705	0.00721	0.02019	0.00058	322	56	139	6	129	4
HS09-14	0.79	0.04858	0.00040	0.13516	0.00259	0.02017	0.00035	128	119	129	2	129	2
HS09-15	0.99	0.04871	0.00031	0.13158	0.00213	0.01959	0.00028	200	17	126	2	125	2
HS09-16	1.02	0.04959	0.00093	0.13639	0.00391	0.01993	0.00032	176	44	130	4	127	2

(Continued)

**Table 1.** (Continued)

Spots	Th/U	<sup>207</sup> Pb/ <sup>206</sup> Pb		<sup>207</sup> Pb/ <sup>235</sup> U		<sup>206</sup> Pb/ <sup>238</sup> U		<sup>207</sup> Pb/ <sup>206</sup> Pb		<sup>207</sup> Pb/ <sup>235</sup> U		<sup>206</sup> Pb/ <sup>238</sup> U	
		Ratio	1σ	Ratio	1σ	Ratio	1σ	Ma	1σ	Ma	1σ	Ma	1σ
HS09-17	0.90	0.05245	0.00110	0.14782	0.00526	0.02040	0.00044	306	31	140	5	130	3
HS09-18	0.82	0.04873	0.00037	0.13456	0.00264	0.02003	0.00039	200	17	128	2	128	2
HS09-19	0.73	0.04865	0.00036	0.13296	0.00232	0.01982	0.00033	132	114	127	2	127	2
HS09-20	0.79	0.04985	0.00047	0.13416	0.00250	0.01952	0.00035	187	8	128	2	125	2

the Plesovice zircon during our analyses, completely consistent with the recommended ages ( $337.13 \pm 0.37$  Ma, Sláma *et al.* 2008).

*In situ* zircon Hf isotope measurements were subsequently taken on the same spots previously analysed for U–Pb dating. Zircon Hf isotopes were analysed using a GeoLasPro 193 nm laser ablation microprobe that was attached to a Neptune multi-collector ICP-MS at the Institute of Geology, Chinese Academy of Geological Sciences, Beijing, China. The instrumental conditions and data acquisition were similar to those described by Zhao *et al.* (2012). A 44 μm laser beam was used for *in situ* Hf isotope analysis. Helium was used as a carrier gas in the ablation cell. The <sup>176</sup>Lu/<sup>175</sup>Lu ratio of 0.02655 (Vervoort *et al.* 2004) and <sup>176</sup>Yb/<sup>173</sup>Yb ratio of 0.796218 (Chu *et al.* 2002) were used to correct the isobaric interferences of <sup>176</sup>Lu and <sup>176</sup>Yb on <sup>176</sup>Hf. Yb isotope ratios were normalized to a <sup>172</sup>Yb/<sup>173</sup>Yb ratio of 1.35274 (Chu *et al.* 2002) and Hf isotope ratios to a <sup>179</sup>Hf/<sup>177</sup>Hf ratio of 0.7325 (Wu *et al.* 2006) for instrumental mass bias correction. Zircon GJ1 was used as the reference standard during our routine analyses, with a weighted mean <sup>176</sup>Hf/<sup>177</sup>Hf ratio of  $0.282007 \pm 0.000007$  ( $2\sigma$ ,  $n = 36$ ) (the recommended value is  $0.282000 \pm 0.000005$ , Morel *et al.* 2008). A decay constant value of  $1.867 \times 10^{-11} \text{ a}^{-1}$  for <sup>176</sup>Lu (Soderlund *et al.* 2004), the present-day chondritic ratios of <sup>176</sup>Hf/<sup>177</sup>Hf = 0.282785 and <sup>176</sup>Lu/<sup>177</sup>Hf = 0.0336 (Bouvier *et al.* 2008) were adopted to calculate εHf values. The depleted mantle Hf model age (single-stage model age,  $T_{\text{DM1}}$ ) was calculated in reference to the depleted-mantle source with the present-day <sup>176</sup>Hf/<sup>177</sup>Hf ratio of 0.28325 and <sup>176</sup>Lu/<sup>177</sup>Hf of 0.0384 (Griffin *et al.* 2000). The ‘crust’ Hf model age (two-stage model,  $T_{\text{DM2}}$ ) was calculated with respect to the average continental crust with a <sup>176</sup>Lu/<sup>177</sup>Hf value of 0.015 (Griffin *et al.* 2002).

### 3.c. Whole-rock geochemistry

On the basis of the petrographical studies, 16 of the freshest representative rock samples from the Wuzhangshan and Huashan intrusions were selected for whole-rock major-, trace- and rare earth element (REE) analyses. Rock samples were crushed in steel crushers and grinded in an agate mill to a grain size of <200 mesh. Major elements were analysed using standard X-ray fluorescence (XRF), except for the FeO content analysed with the potassium bichromate titrimetric method (Andrade *et al.* 2002), at the Analytical Laboratory of Beijing Research Institute of Uranium Geology, Beijing. Accuracies of XRF analyses are better than 2 %. Trace elements and REE were determined by ICP-MS at the Analytical Laboratory of Beijing Research Institute of Uranium Geology, Beijing, following digestion of sample powder (~0.05 g) in an HF + HNO<sub>3</sub> (8:3) solution, drying and second dissolution in 3 mL HNO<sub>3</sub>. Rh was used as an internal standard to monitor signal drift during counting. The analytical precision of ICP-MS analyses is better than 5 % with internal standards.

### 3.d. Whole-rock Sr–Nd isotopes

The whole rock Rb–Sr and Sm–Nd isotopic analyses were measured using an IsoProbe-T TI Mass Spectrometer at the Analytical Laboratory of the Beijing Research Institute of Uranium Geology, Beijing, China, following procedures similar to those of Zhao *et al.* (2012). Samples of ~100 mg were spiked and dissolved in screw-top Teflon containers with HF and HNO<sub>3</sub>. Mass fractionation corrections for Sr and Nd isotopic ratios were based on values of <sup>86</sup>Sr/<sup>88</sup>Sr = 0.1194 and <sup>146</sup>Nd/<sup>144</sup>Nd = 0.7219 (Rasskazov *et al.* 2010). During a long period of analysis, the <sup>87</sup>Sr/<sup>86</sup>Sr ratio of the Sr NBS-987 standard and the <sup>143</sup>Nd/<sup>144</sup>Nd ratio of the Nd La Jolla standard were  $0.710215 \pm 11$  ( $2\sigma$ ,  $n = 22$ ) (the literature value is 0.710215, Nyquist *et al.* 1994) and  $0.511852 \pm 4$  ( $2\sigma$ ,  $n = 24$ ) (the literature value is 0.511860, Nyquist *et al.* 1994), respectively. Decay constant values of  $1.393 \times 10^{-11} \text{ a}^{-1}$  for <sup>87</sup>Rb (Nebel *et al.* 2011) and  $6.54 \times 10^{-12} \text{ a}^{-1}$  for <sup>147</sup>Sm (Lugmair & Marti, 1978), the present-day chondritic ratios of <sup>147</sup>Sm/<sup>144</sup>Nd = 0.1967 (Jacobsen & Wasserburg, 1980) and the present day depleted-mantle ratios of <sup>143</sup>Nd/<sup>144</sup>Nd = 0.513151 and <sup>147</sup>Sm/<sup>144</sup>Nd = 0.2136 (Liew & Hofmann, 1988) were adopted to calculate (<sup>87</sup>Sr/<sup>86</sup>Sr)*t* and Nd model ages.

## 4. Results

### 4.a. Zircon U–Pb geochronology

Two samples from the Wuzhangshan and Huashan plutons were chosen for LA-ICP-MS zircon U–Pb dating. The results are listed in Table 1. Representative CL images of the zircons in this study are shown in Figure S2 and S3 (in Supplementary Material at <https://doi.org/10.1017/S0016756819000888>) and the age data are plotted in Figure 3.

Sample WZS03 (34°12′28″ N, 111°41′50″ E) is a porphyritic monzogranite collected from the Wuzhangshan pluton. Zircon grains from this sample are light yellow to colourless, euhedral and short prismatic shape, with a length of 100–300 μm and a length-to-width ratio of 1.5:1 to 3:1 (Fig. S2 in Supplementary Material at <https://doi.org/10.1017/S0016756819000888>). Most grains show obvious oscillatory zoning in CL images and have high Th/U ratios ranging from 0.22 to 0.99 (Table 1), indicating magmatic origin. Thirteen of nineteen spots have concordant ages between 160 Ma and 162 Ma (Fig. 3a, b), with a weighted mean <sup>206</sup>Pb/<sup>238</sup>U age of  $160.7 \pm 0.6$  Ma ( $n = 13$ , MSWD = 0.52), which is interpreted to be the crystallization age. Some zircons contain an inner core (Fig. S2 in Supplementary Material at <https://doi.org/10.1017/S0016756819000888>). Three spots are analysed from the core domains (WZS-LH01, 02, 03) and yield old <sup>207</sup>Pb/<sup>206</sup>Pb ages of  $2465 \pm 5$  Ma,  $1915 \pm 43$  Ma,  $2032 \pm 24$  Ma, respectively, which are interpreted as inherited zircons.

Sample HS09 (34°21′45″ N, 111°35′16″ E) is a porphyritic monzogranite collected from the Huashan pluton. Zircon grains from

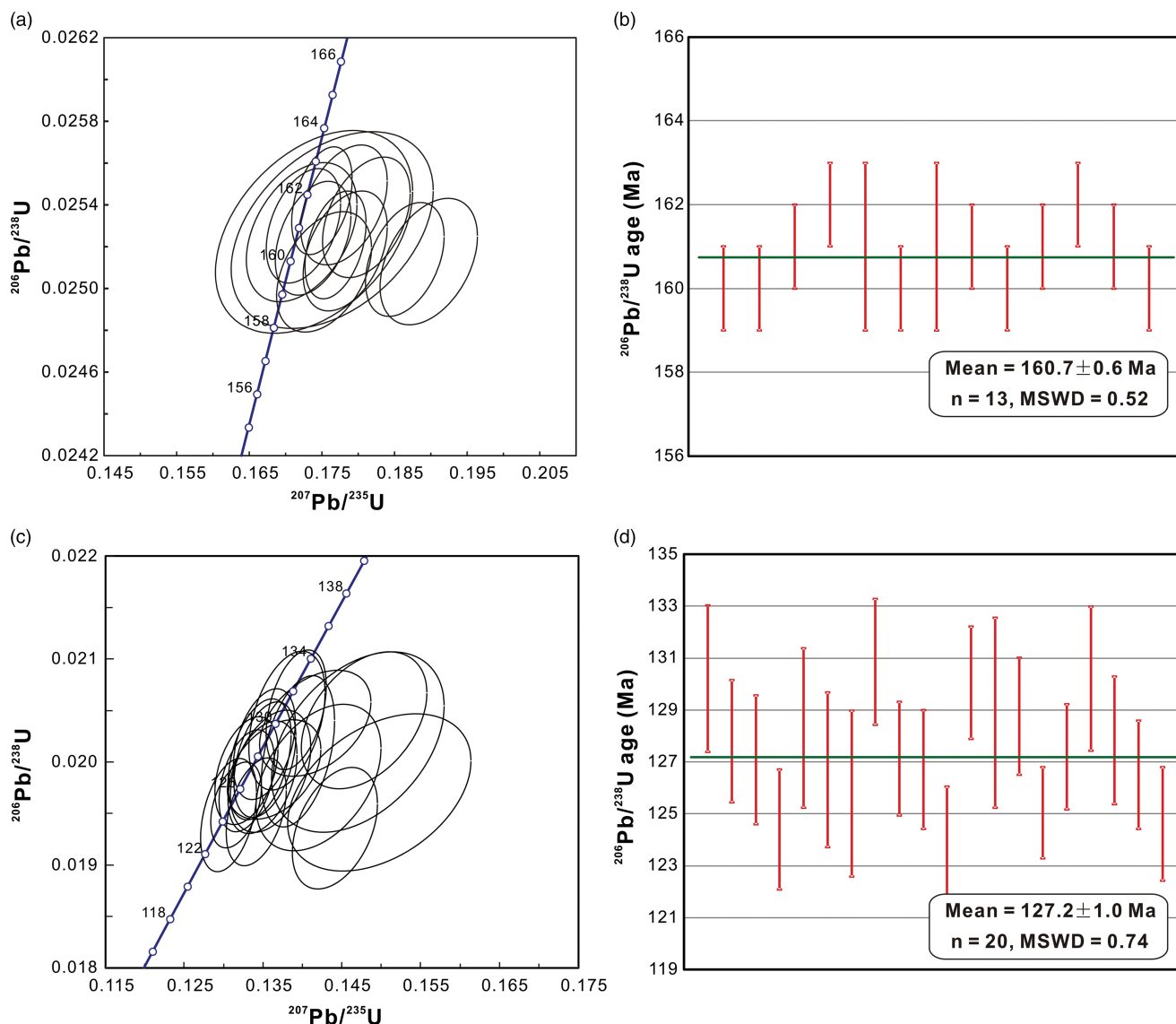


Fig. 3. (Colour online) Zircon U–Pb concordia and average age diagrams for sample WZS03 from the Wuzhangshan pluton (a, b) and sample HS09 from the Huashan pluton (c, d).

this sample are colourless, transparent and euhedral, with a length of 60–200  $\mu\text{m}$  and a length-to-width ratio of 2:1 to 3:1 (Fig. S3 in Supplementary Material at <https://doi.org/10.1017/S0016756819000888>). They show pyramid termination with clear oscillatory growth zoning and have high Th/U ratios (0.72–1.13, Table 1), suggesting a magmatic origin. All 20 zircon crystals from sample HS09 are concordant with  $^{206}\text{Pb}/^{238}\text{U}$  ages ranging from  $123.6 \pm 2.5$  Ma to  $130.9 \pm 2.4$  Ma (Fig. 3c, d), giving a weighted mean  $^{206}\text{Pb}/^{238}\text{U}$  age of  $127.2 \pm 1.0$  Ma ( $n = 20$ , MSWD = 0.74).

#### 4.b. Whole-rock geochemistry

Representative major and trace element concentrations of the Wuzhangshan and Huashan intrusive rocks are listed in Table 2. The Wuzhangshan intrusive rocks have a narrow range of  $\text{SiO}_2$ , ranging from 68.3 to 71.6 wt % (Fig. 4a; Table 2), and low MgO contents ranging from 0.15 to 0.55 wt %. They are slightly peraluminous rocks with ACNK values (molar  $\text{Al}_2\text{O}_3/(\text{CaO} + \text{Na}_2\text{O} + \text{K}_2\text{O})$ ) varying from 1.00 to 1.10 (Fig. 4b). All samples lie within the high-K calcalkaline to shoshonite fields (Fig. 4c). The

Wuzhangshan monzogranites are characterized by high Sr (904–1487 ppm) but low Y (12.2–18.9 ppm) and Yb (1.5–2.2 ppm) contents, with elevated Sr/Y (56.5–97.8) and  $(\text{La}/\text{Yb})_{\text{N}}$  (11.8–19.1) ratios, indicative of apparent adakitic characteristics (Fig. 4d). The rocks are strongly enriched in large-ion lithophile elements (e.g. Rb, K, Ba and Sr), and relatively depleted in HFSEs (e.g. Nb, Ta, P and Ti) (Fig. 5). They have total REE concentrations with  $\Sigma\text{REE}$  ranging from 112 ppm to 184 ppm, and are strongly enriched in LREEs and relatively depleted in heavy rare earth elements (HREEs), with LREE/HREE ratio of 11.2–14.0, displaying right-inclined patterns (Fig. 6). The pluton has negligible to slightly positive Eu anomalies ( $\text{Eu}/\text{Eu}^* = 1.0$ –1.4) and shows more pronounced fractionation in LREEs than in HREEs with  $(\text{La}/\text{Sm})_{\text{N}}$  and  $(\text{Dy}/\text{Yb})_{\text{N}}$  ratios of 5.5–8.0 and 0.8–1.0, respectively.

Similar to the Wuzhangshan monzogranites, the Huashan monzogranites are also slightly peraluminous ( $\text{ACNK} = 1.00$ –1.10) and high-K calcalkalic to shoshonitic ( $\text{K}_2\text{O} = 3.75$ –5.62) (Fig. 4b, c). Rocks from the Huashan pluton are also characterized by strong enrichment of light REEs over heavy REEs ( $\text{LREE}/\text{HREE} = 12.1$ –27.2 and  $(\text{La}/\text{Yb})_{\text{N}} = 14.8$ –42.9), weakly differentiated heavy

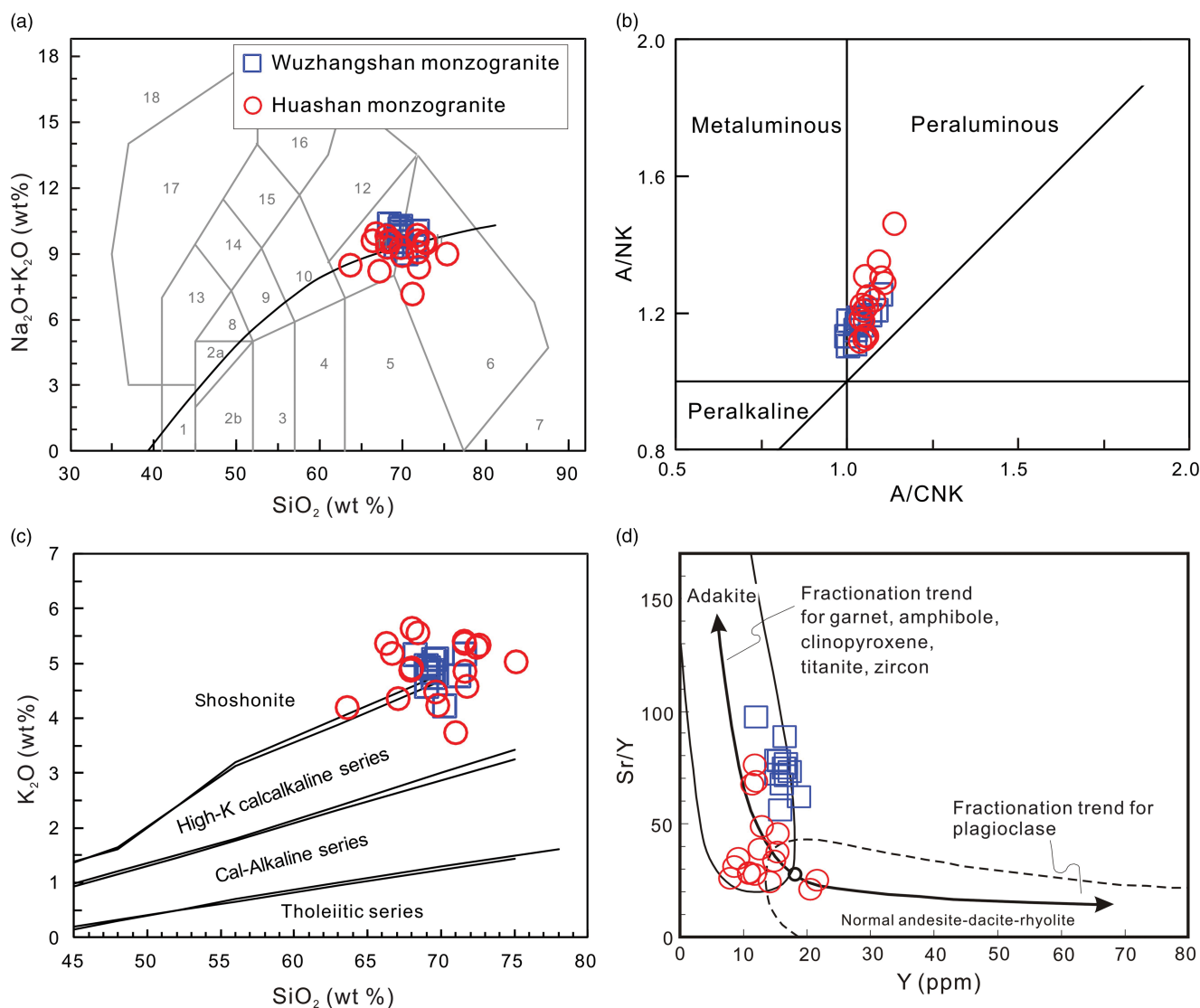


**Fig. 4.** (Colour online) Geochemistry diagrams for the Wuzhangshan and Huashan monzogranites. (a)  $\text{SiO}_2$  vs  $(\text{Na}_2\text{O} + \text{K}_2\text{O})$  classification diagram (after Middlemost, 1994). (b) A/CNK vs A/NK diagram (after Maniar & Piccoli, 1989). (c)  $\text{SiO}_2$  vs  $\text{K}_2\text{O}$  classification diagram (after Peccerillo & Taylor, 1976). (d) Sr/Y vs Y diagram showing adakitic characteristics (after Defant & Drummond, 1990).

REEs ( $(\text{Dy}/\text{Yb})_N = 0.90\text{--}1.50$ ), pronounced negative anomalies in HFSEs (e.g. Nb, Ta, P and Ti) and remarkable enrichment in large-ion lithophile elements (e.g. Rb, K and Ba) (Fig. 5). However, compared to the Wuzhangshan rocks, the Huashan monzogranites have a wider range of  $\text{SiO}_2$ , ranging from 63.7 to 75.0 wt %, and higher MgO, Cr, Co and Ni contents, but lower Sr/Y (21.3–76.5) and  $\text{Fe}^{3+}/\text{Fe}^{2+}$  (0.64–1.12) (Fig. 7c). Binary element and ratio vs  $\text{SiO}_2$  variation diagrams (Fig. 7d, e, f) show linear trends. The Huashan monzogranites have zero to weak negative Eu anomalies ( $\text{Eu}/\text{Eu}^* = 0.6\text{--}1.0$ , except for two samples) and elevated  $10,000 \times \text{Ga}/\text{Al}$  values. In Figure 8, more than half of the samples from the Huashan monzogranites plot in the ‘A-type granites’ field, and the remaining samples fall near the contact line between the I- and S-type granites field and the ‘A-type granite’ field.

#### 4.c. Zircon Hf isotopes

*In situ* zircon Hf analyses of samples from the Wuzhangshan and Huashan plutons are listed in Table 3 and shown in Figure 9. Zircons from the Wuzhangshan pluton have  $^{176}\text{Lu}/^{177}\text{Hf}$  ratios

of 0.001451 to 0.003028 and  $^{176}\text{Hf}/^{177}\text{Hf}$  ratios of 0.281639 to 0.281973. These results yield  $\epsilon\text{Hf}(t)$  values of  $-37.12$  to  $-25.35$ , with a mean of  $-28.14$ , corresponding to two-stage Hf model ages of 3502 Ma to 2773 Ma (mostly between 2931 Ma and 2773 Ma). One inherited zircon grain shows much lower signature with  $^{176}\text{Hf}/^{177}\text{Hf}$  ratios of 0.281189, and  $\epsilon\text{Hf}(t = 2465 \text{ Ma})$  value of  $-1.8$ , which is consistent with that of the TTG gneisses of the Taihua Group (Fig. 9). The calculated single-stage and two-stage model ages of the inherited zircon grain are 2857 Ma and 3903 Ma, respectively, which is close to the  $^{207}\text{Pb}/^{206}\text{Pb}$  age of the analysed inherited zircon. Zircons from the Huashan pluton show homogeneous  $^{176}\text{Hf}/^{177}\text{Hf}$  ratios of 0.282345 to 0.282426, and have  $\epsilon\text{Hf}(t)$  values ranging from  $-12.79$  to  $-9.91$ , which yield two-stage model ages of 1961 Ma to 1781 Ma.

#### 4.d. Whole-rock Sr-Nd isotopes

Samples from the Wuzhangshan pluton have  $^{87}\text{Rb}/^{86}\text{Sr}$  ratios of 0.2628–0.4547 and  $^{87}\text{Sr}/^{86}\text{Sr}$  ratios of 0.7077–0.7086, which correspond to  $(^{87}\text{Sr}/^{86}\text{Sr})_t$  values ranging from 0.7068 to 0.7076



**Table 2.** Major (wt %) and trace element (ppm) concentrations of the Wuzhangshan and Huashan plutons in the Xiong'ershan area

Samples	Wuzhangshan monzogranites												Huashan monzogranites		
	WZS01	WZS02	WZS03	WZS04	WZS05	WZS06	WZS07	WZS08	WZS09	WZS10	WZST01	WZST02	HS01	HS03	HS09
SiO <sub>2</sub>	69.17	69.42	71.20	69.71	68.28	69.63	69.02	69.49	69.52	71.59	70.25	69.04	67.14	71.61	71.59
TiO <sub>2</sub>	0.33	0.29	0.21	0.28	0.29	0.29	0.30	0.26	0.28	0.19	0.26	0.31	0.55	0.20	0.21
Al <sub>2</sub> O <sub>3</sub>	15.24	15.88	15.19	15.64	15.84	15.40	15.52	15.77	15.75	14.95	15.48	14.92	14.86	14.27	14.35
Fe <sub>2</sub> O <sub>3</sub> <sup>T</sup>	2.65	2.17	1.70	1.97	2.20	1.84	2.25	1.79	2.13	1.50	2.50	2.83	4.14	1.67	1.63
MnO	0.07	0.07	0.05	0.06	0.06	0.04	0.06	0.06	0.05	0.06	0.07	0.08	0.09	0.06	0.07
MgO	0.50	0.28	0.26	0.32	0.34	0.24	0.28	0.40	0.21	0.15	0.44	0.55	1.35	0.43	0.34
CaO	2.09	1.75	1.58	1.72	2.05	1.54	1.99	2.02	1.84	1.25	1.93	2.39	2.85	1.63	1.00
Na <sub>2</sub> O	4.55	4.88	4.48	4.80	5.08	5.20	4.78	4.95	4.96	4.76	4.70	4.66	3.81	4.15	4.15
K <sub>2</sub> O	4.91	4.83	4.77	5.07	5.15	4.93	4.95	4.74	5.06	5.16	4.23	4.58	4.36	4.85	5.35
P <sub>2</sub> O <sub>5</sub>	0.10	0.08	0.05	0.08	0.07	0.08	0.07	0.09	0.07	0.04	0.10	0.14	0.26	0.09	0.07
LOI	0.38	0.35	0.49	0.35	0.59	0.76	0.75	0.42	0.13	0.32	0.23	0.48	0.54	0.48	0.65
Total	99.98	100.00	99.99	99.99	99.96	99.95	99.96	99.99	99.99	99.97	100.19	99.98	99.95	99.44	99.42
FeO	0.96	0.93	0.63	0.56	0.80	0.46	0.71	0.90	0.47	0.47	1.08	1.11	1.91	0.91	0.81
Cr	1.43	8.11	0.81	3.26	4.90	1.51	3.14	0.98	0.87	1.07	4.36	4.70	4.91	2.11	1.25
Co	3.10	2.00	1.34	2.22	1.89	1.62	1.93	1.71	1.52	1.08	3.31	3.95	9.47	2.47	1.25
Ni	2.37	2.16	1.35	2.05	2.10	1.89	1.98	1.88	1.53	1.37	2.23	2.53	2.93	1.11	0.71
Ba	2199	2572	2186	2793	3030	3023	2916	2429	2617	2504	2268	2352	974	764	1136
Rb	142	137	142	144	135	114	143	133	144	152	121	123	161	246	242
Th	26.30	15.40	16.40	15.10	12.50	22.20	17.00	20.10	20.90	21.40	17.15	13.05	16.50	18.00	17.30
Nb	19.50	19.70	19.30	16.60	18.60	18.70	19.70	18.60	17.70	18.40	20.35	20.46	21.20	16.00	33.80
Ta	0.79	0.82	0.87	0.68	0.75	0.74	0.78	0.75	0.75	0.74	0.80	0.84	1.32	1.12	1.92
Sr	1212	1303	904	1238	1487	1115	1287	1211	1247	1193	1106	1182	551	329	275
Y	16.90	16.90	16.00	15.80	16.70	15.40	17.50	15.40	16.60	12.20	16.25	18.96	21.80	9.40	8.77
Ga	17.10	16.30	15.80	15.60	15.30	16.00	15.50	15.30	16.00	14.60	17.28	17.31	18.80	17.40	23.30
La	49.20	36.70	34.40	47.30	35.50	37.70	38.20	34.00	44.30	31.00	33.96	47.74	50.90	26.50	52.60
Ce	72.10	58.20	55.60	64.50	55.30	57.10	60.80	54.00	63.00	46.70	59.27	79.40	85.10	41.80	90.80
Pr	7.52	6.40	6.02	6.85	6.09	6.23	6.69	5.92	6.89	5.03	6.46	8.33	9.46	4.20	9.43
Nd	26.00	22.30	21.00	23.50	21.90	22.40	23.60	20.70	23.80	17.30	22.42	29.45	34.90	14.40	31.90
Sm	3.97	3.74	3.38	3.88	3.69	3.75	3.93	3.43	3.90	3.62	3.57	4.49	5.84	2.33	4.37
Eu	1.38	1.38	1.14	1.42	1.40	1.37	1.48	1.30	1.41	1.10	1.29	1.48	1.40	0.63	0.86
Gd	3.36	3.01	2.84	3.17	3.12	3.14	3.26	2.83	3.14	2.23	3.19	4.07	4.97	1.95	3.27
Tb	0.53	0.50	0.47	0.51	0.51	0.49	0.57	0.47	0.51	0.35	0.48	0.59	0.82	0.34	0.45
Dy	2.77	2.64	2.50	2.65	2.65	2.52	2.86	2.40	2.59	1.79	2.59	3.17	4.01	1.54	1.81
Ho	0.55	0.53	0.51	0.52	0.55	0.49	0.58	0.48	0.53	0.37	0.53	0.62	0.76	0.32	0.30
Er	1.66	1.68	1.59	1.55	1.69	1.51	1.74	1.51	1.67	1.14	1.59	1.76	2.00	0.83	0.77
Tm	0.30	0.29	0.31	0.28	0.29	0.28	0.32	0.28	0.30	0.22	0.32	0.34	0.34	0.16	0.13
Yb	1.98	2.03	2.10	1.78	1.94	1.88	2.15	1.97	2.03	1.50	2.00	2.22	2.33	1.14	0.88
Lu	0.31	0.32	0.36	0.28	0.31	0.30	0.33	0.32	0.33	0.25	0.32	0.36	0.35	0.19	0.13
ΣREE	171.6	139.7	132.2	158.2	134.9	139.2	146.5	129.6	154.4	111.6	138.0	184.0	203.2	96.3	197.7
LREE/HREE	13.98	11.71	11.40	13.73	11.21	12.11	11.41	11.63	12.91	13.23	11.52	13.02	12.05	13.91	24.52
(La/Yb) <sub>N</sub>	17.82	12.97	11.75	19.06	13.13	14.38	12.74	12.38	15.65	14.82	12.18	15.43	15.67	16.67	42.92

(Continued)

Table 2. (Continued)

Samples	Wuzhangshan monzogranites												Huashan monzogranites		
	WZS01	WZS02	WZS03	WZS04	WZS05	WZS06	WZS07	WZS08	WZS09	WZS10	WZST01	WZST02	HS01	HS03	HS09
(La/Sm)N	8.00	6.33	7.87	6.21	6.49	6.28	6.40	6.57	7.33	5.53	6.14	6.86	5.63	7.34	7.77
(Dy/Yb)N	0.94	0.87	1.00	0.91	0.90	0.89	0.82	0.80	0.85	0.80	0.87	0.96	1.15	0.90	1.38
$\delta\text{Eu}$	1.13	1.22	1.09	1.20	1.23	1.19	1.23	1.24	1.19	1.36	1.14	1.04	0.77	0.87	0.67
Sr/Y	71.7	77.1	56.5	78.4	89.0	72.4	73.5	78.6	75.1	97.8	68.1	62.3	25.3	35.0	31.4
$\text{Fe}^{3+}/\text{Fe}^{2+}$	1.47	1.09	2.15	1.46	2.59	1.84	0.78	1.42	3.07	1.86	1.07	1.28	0.94	0.64	0.80
ANK	1.19	1.20	1.17	1.14	1.11	1.17	1.19	1.21	1.16	1.11	1.26	1.18	1.35	1.18	1.14
ACNK	1.04	1.07	1.05	1.00	1.01	1.03	1.04	1.09	1.03	1.03	1.10	1.01	1.09	1.05	1.06
Samples	Huashan monzogranites														
	HS11	HS12	HS16	HST01	HST02	HST03	HST04	HST05	HST06	HST07	HST08	HST09	HST10	HST11	
SiO <sub>2</sub>	63.73	67.98	69.79	70.99	66.74	68.05	71.75	69.65	68.46	68.07	75.04	72.56	72.40	71.56	
TiO <sub>2</sub>	0.52	0.27	0.29	0.50	0.27	0.35	0.30	0.25	0.33	0.40	0.16	0.22	0.23	0.20	
Al <sub>2</sub> O <sub>3</sub>	16.81	16.42	15.71	12.69	17.28	15.51	13.49	14.97	15.32	15.22	13.37	13.99	14.33	14.80	
Fe <sub>2</sub> O <sub>3</sub> <sup>T</sup>	4.43	2.11	2.35	4.01	2.29	2.99	2.56	2.14	2.36	3.55	1.50	1.62	1.83	1.62	
MnO	0.09	0.07	0.07	0.08	0.05	0.07	0.07	0.07	0.07	0.07	0.05	0.06	0.07	0.05	
MgO	1.57	0.36	0.40	1.30	0.79	0.96	0.81	0.45	0.85	1.09	0.31	0.38	0.39	0.35	
CaO	3.59	2.15	2.18	2.57	2.70	2.41	1.85	1.91	2.11	2.36	0.92	1.06	1.07	1.14	
Na <sub>2</sub> O	4.23	4.84	4.61	3.42	4.64	4.30	3.76	4.72	3.97	3.84	3.90	4.08	4.17	4.35	
K <sub>2</sub> O	4.20	4.87	4.24	3.75	5.17	4.91	4.58	4.48	5.54	5.62	5.02	5.32	5.28	5.39	
P <sub>2</sub> O <sub>5</sub>	0.28	0.09	0.09	0.24	0.17	0.21	0.17	0.13	0.18	0.24	0.07	0.11	0.11	0.09	
LOI	0.52	0.29	0.22	0.35	0.54	0.48	0.56	1.00	0.79	0.49	0.89	0.76	0.40	0.57	
Total	99.96	99.45	99.95	99.90	100.6	100.2	99.90	99.77	99.98	101.0	101.2	100.2	100.3	100.1	
FeO	2.38	0.89	1.25	1.90											
Cr	5.96	1.70	1.81	6.25	2.57	3.06	2.82	0.81	3.71	3.13	0.36	0.93	0.82	1.32	
Co	9.10	1.90	1.93	7.04	4.32	8.63	3.84	2.38	4.07	6.71	0.96	1.14	1.37	1.24	
Ni	3.07	0.98	0.94	3.41	1.72	1.50	1.57	0.71	1.89	1.77	0.56	0.56	0.27	0.24	
Ba	1170	2144	1801	877	1608	928	677	1462	1075	1433	705	1072	1088	1113	
Rb	136	167	139	162	167	186	257	182	227	199	207	217	224	219	
Th	9.11	10.30	13.70	20.32	15.54	22.70	29.90	13.63	19.50	15.87	26.02	20.66	21.82	21.61	
Nb	14.70	20.90	24.80	19.47	15.59	16.86	22.45	18.78	15.11	15.48	26.04	31.63	36.00	33.96	
Ta	0.75	0.88	1.03	1.39	1.44	1.18	1.60	0.86	0.87	0.92	1.29	1.59	2.18	1.74	
Sr	718	918	844	441	788	509	352	645	499	588	213	314	318	334	
Y	15.60	12.00	12.20	20.74	11.60	15.04	14.35	13.11	12.75	15.56	8.14	11.10	11.09	11.99	
Ga	19.20	20.70	19.80	16.80	20.12	18.72	18.78	22.21	19.46	19.09	22.71	24.22	24.17	25.53	
La	40.20	47.10	52.10	50.39	24.61	37.21	38.43	39.62	49.51	30.17	41.50	53.87	54.45	52.78	
Ce	62.70	79.80	87.20	90.35	43.76	63.43	63.94	70.49	66.31	59.45	73.55	96.18	99.49	94.37	
Pr	6.56	8.61	9.36	9.98	4.67	6.50	6.38	7.42	5.97	6.44	6.98	9.64	10.07	9.49	
Nd	23.20	30.40	33.50	36.23	16.53	23.27	22.34	26.61	20.64	23.03	23.04	31.42	33.99	31.50	
Sm	3.67	4.30	4.85	5.86	2.75	3.89	3.52	3.84	3.31	3.88	2.64	4.22	4.52	4.50	
Eu	1.02	1.21	1.29	1.25	1.02	1.01	0.88	1.00	1.04	1.14	0.56	0.82	0.88	0.92	
Gd	3.17	3.58	3.78	4.69	2.24	3.05	2.77	3.02	2.85	3.23	2.14	3.10	3.26	3.26	
Tb	0.50	0.50	0.54	0.71	0.32	0.45	0.41	0.39	0.38	0.46	0.28	0.41	0.42	0.43	
Dy	2.45	2.17	2.28	3.73	1.89	2.44	2.33	2.14	2.00	2.52	1.19	1.97	1.91	2.09	

(Continued)

Table 2. (Continued)

Samples	Huashan monzogranites													
	HS11	HS12	HS16	HST01	HST02	HST03	HST04	HST05	HST06	HST07	HST08	HST09	HST10	HST11
Ho	0.47	0.39	0.37	0.72	0.36	0.47	0.44	0.40	0.38	0.47	0.24	0.34	0.35	0.36
Er	1.33	1.01	0.98	2.04	1.00	1.29	1.29	1.04	1.01	1.28	0.63	0.98	0.93	1.02
Tm	0.22	0.15	0.15	0.35	0.16	0.21	0.21	0.17	0.17	0.19	0.10	0.14	0.14	0.15
Yb	1.63	1.00	1.02	2.48	1.19	1.46	1.61	1.13	1.22	1.42	0.75	1.07	1.08	1.03
Lu	0.26	0.15	0.14	0.36	0.19	0.26	0.29	0.18	0.19	0.22	0.13	0.16	0.18	0.15
ΣREE	147.7	180.4	197.6	209.1	100.7	144.9	144.8	157.5	155.0	133.9	153.7	204.3	211.7	202.1
LREE/HREE	13.73	19.15	20.33	12.87	12.70	14.05	14.49	17.59	17.90	12.68	27.16	24.01	24.59	22.80
(La/Yb) <sub>N</sub>	17.69	33.89	36.64	14.57	14.83	18.28	17.12	25.15	29.11	15.24	39.69	36.11	36.16	36.76
(La/Sm) <sub>N</sub>	7.07	7.07	6.93	5.55	5.78	6.18	7.05	6.66	9.66	5.02	10.15	8.24	7.78	7.57
(Dy/Yb) <sub>N</sub>	1.01	1.46	1.50	1.01	1.06	1.12	0.97	1.27	1.10	1.19	1.06	1.23	1.18	1.36
δEu	1.15	0.92	0.89	0.71	1.22	0.86	0.83	0.87	1.01	0.96	0.70	0.66	0.67	0.70
Sr/Y	46.0	76.5	69.2	21.26	67.93	33.84	24.53	49.20	39.14	37.79	26.17	28.29	28.67	27.86
Fe <sup>3+</sup> /Fe <sup>2+</sup>	0.66	1.12	0.68	0.89										
ANK	1.46	1.24	1.29	1.31	1.31	1.25	1.21	1.19	1.22	1.23	1.13	1.12	1.14	1.14
ACNK	1.14	1.08	1.11	1.06	1.10	1.06	1.05	1.04	1.06	1.05	1.05	1.04	1.06	1.06

A/CNK = molar Al<sub>2</sub>O<sub>3</sub>/(CaO + Na<sub>2</sub>O + K<sub>2</sub>O); A/NK = molar Al<sub>2</sub>O<sub>3</sub>/(Na<sub>2</sub>O + K<sub>2</sub>O); δEu = ω(Eu)<sub>N</sub>/[(1/2)(ω(Sm)<sub>N</sub> + ω(Gd)<sub>N</sub>)]]; data of WZST01-02 and HST01-11 are from Han *et al.* (2007) and Xiao *et al.* (2012).

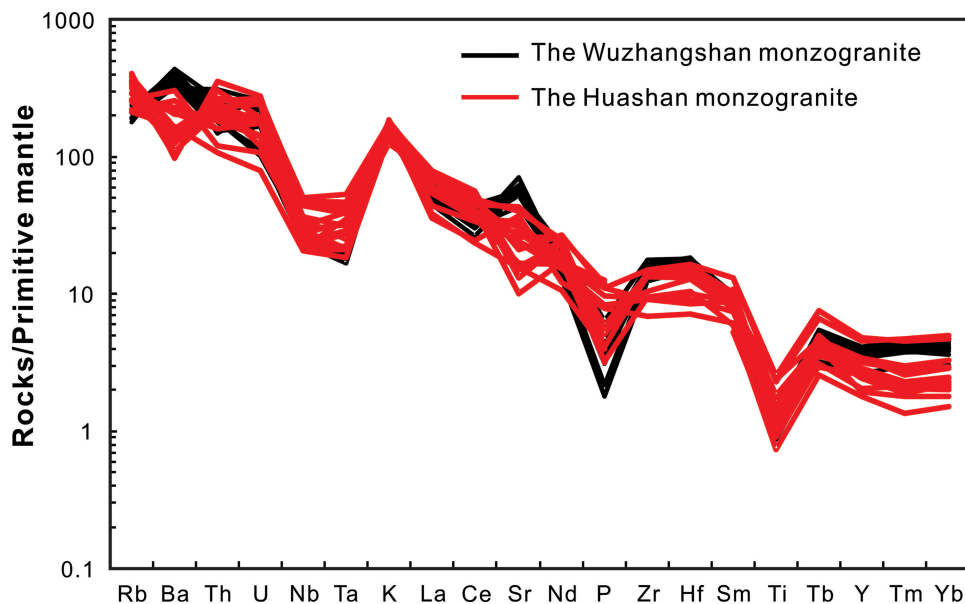


Fig. 5. (Colour online) Primitive mantle - normalized trace element diagram for the Wuzhangshan and Huashan monzogranites in the Xiong'er shan area. Primitive mantle values from Sun & McDonough (1989).

(Table 4). The samples show <sup>147</sup>Sm/<sup>144</sup>Nd ratios of 0.0915–0.1019 and <sup>143</sup>Nd/<sup>144</sup>Nd ratios of 0.5115–0.5116, which yield εNd(*t*) values ranging from –21.0 to –19.1, and two-stage Nd model ages of 2491–2646 Ma. The felsic rocks coeval with Huashan monzogranite in the Xiong'er shan and its adjacent areas have (<sup>87</sup>Sr/<sup>86</sup>Sr)<sub>*t*</sub> values ranging from 0.7070 to 0.7138 and εNd(*t*) values from –16.4 to –7.8, with two-stage Nd model ages of 2268–1549 Ma (Gao *et al.* 2010, 2014; Cao *et al.* 2016).

## 7. Discussion

### 7.a. Multiple stages of magmatism during Late Jurassic to Early Cretaceous in the Xiong'er shan area

The Wuzhangshan and Huashan plutons have different zircon U–Pb ages, major and trace elemental and Sr–Nd–Hf isotopic compositions, indicating that they were generated from different magmatic sources and potentially in different tectonic

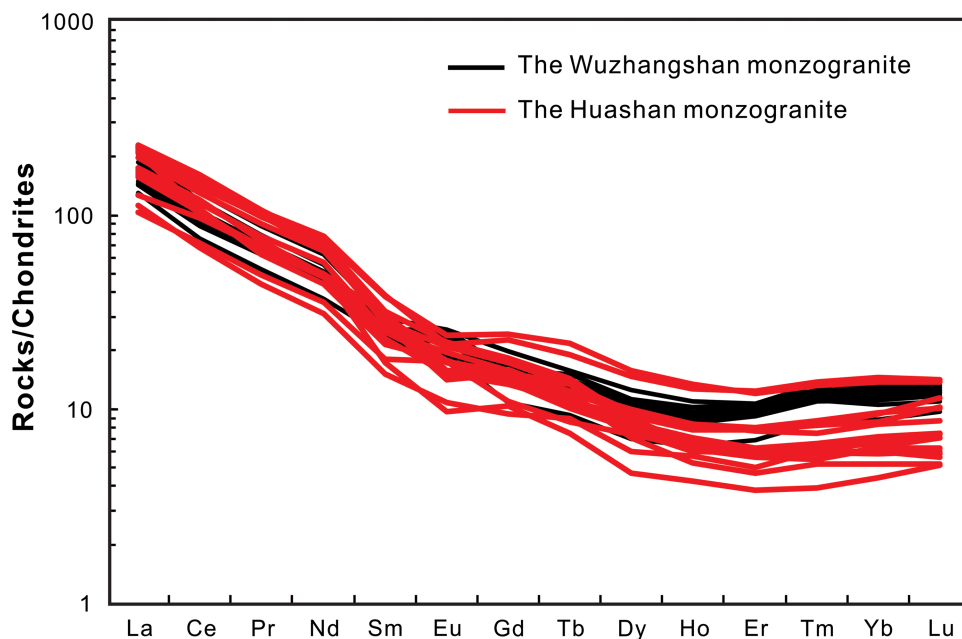


**Fig. 6.** (Colour online) Chondrite-normalized rare earth element patterns for the Wuzhangshan and Huashan monzogranites in the Xiong'ershan area. Chondrite values from Sun & McDonough (1989).

environments (Pearce, 1996). Identification of multiple stages of magmatism in the Xiong'ershan area is important for evaluating the geodynamics of this region and understanding the genesis of magmatic rocks and associated ore deposits. In order to further identify magmatic stages during the Late Jurassic to Early Cretaceous in the Xiong'ershan area, published zircon U–Pb ages for the plutons in this region from the recent literature are collected and listed in Table S1 in the Supplementary Material at <https://doi.org/10.1017/S0016756819000888>. Our new data, in combination with these available data, suggest that the late Mesozoic magmatic event in the Xiong'ershan area mainly took place in 165–113 Ma, lasting for nearly 50 Ma. These zircon U–Pb ages (Fig. 10) also indicate that the magmatism during the Late Jurassic to Early Cretaceous in the Xiong'ershan area can be divided into at least two episodes: 165–150 Ma (early episode) and 138–113 Ma (late episode). The Wuzhangshan and Huashan plutons are the two largest batholiths in the Xiong'ershan area (Fig. 1c). New high-precision zircon U–Pb dates obtained from these two batholiths indicate that the Wuzhangshan and Huashan monzogranites were emplaced at *c.* 160 Ma and 127 Ma, respectively. These features indicate that the monzogranites from the Wuzhangshan and Huashan probably preserve the imprints of the two magmatic episodes during the Late Jurassic to Early Cretaceous in the Xiong'ershan area, respectively.

### 7.b. Petrogenesis of the magmas and their signatures

The geochemical characteristics of the Wuzhangshan monzogranites (e.g. enrichment in LREE with high Sr/Y and La/Yb ratios and without negative Eu anomalies) are similar to those of adakites or adakitic-like rocks. Theories to account for the origin of adakites and adakitic-like rocks include (1) partial melting of a subducting slab (e.g. Defant & Drummond, 1990; Martin *et al.* 2005); (2) crustal assimilation and fractional crystallization (AFC) processes from parental basaltic magmas (e.g. Castillo *et al.* 1999; Du *et al.* 2018); (3) partial melting of mafic rocks in the lower part of a

thickened crust (e.g. Petford & Atherton, 1996; Tang *et al.* 2017); (4) partial melting of delaminated lower crust (e.g. Gao *et al.* 2004; Wang *et al.* 2006).

As there is little geodynamic evidence for the existence of contemporaneous subduction in the wider region around the Xiong'ershan area, combined with the observation that the Wuzhangshan monzogranites have negative  $\epsilon\text{Nd}(t)$  and  $\epsilon\text{Hf}(t)$  values with Archaean–Palaeoproterozoic model ages (Tables 3, 4), we conclude that the Wuzhangshan monzogranites are unlikely to have been produced by partial melting of subducted crust. Crustal AFC processes from contemporaneous basaltic magma also seem unlikely to produce the Wuzhangshan monzogranites because no coeval basaltic rocks (165–150 Ma) have been found in the Xiong'ershan area. No changes in Sr, Sr/Y and  $\delta\text{Eu}$  values as  $\text{SiO}_2$  increases (Fig. 7d, e, f) suggests that the adakitic geochemical characteristics of the Wuzhangshan monzogranites are probably inherited from the magmatic source, and are not produced by fractional crystallization. On a plot of the La/Yb vs Yb (Fig. 11), the data from the Wuzhangshan pluton are consistent with a partial melting trend (White, 2013). Moreover, the Wuzhangshan pluton has a wide variety of chemical composition but a very narrow range in Sr–Nd–Hf isotopes (Figs 9, 12). These features not only provide further support for the idea that AFC processes could not have produced the geochemical variation within the Wuzhangshan monzogranites, but also indicate that partial melting of mafic rocks in the lower part of a thickened crust or delaminated lower crust may be the most likely interpretation for the origin of the Wuzhangshan monzogranites (Van der Meer *et al.* 2018). It is generally believed that the adakitic magmas derived from partial melting of mafic rock in the lower crust should have relatively low MgO, Cr, Co and Ni contents (e.g. Petford & Atherton, 1996; Tang *et al.* 2017), whereas the adakitic magmas produced by dehydration melting of delaminated crustal rocks in the mantle should have elevated MgO, Cr, Co and Ni contents (e.g. Rapp *et al.* 1999; Gao *et al.* 2004; Wang *et al.* 2006), due to the reaction between pure adakitic melts and the mantle peridotite as the pure melts pass through the mantle. The Wuzhangshan

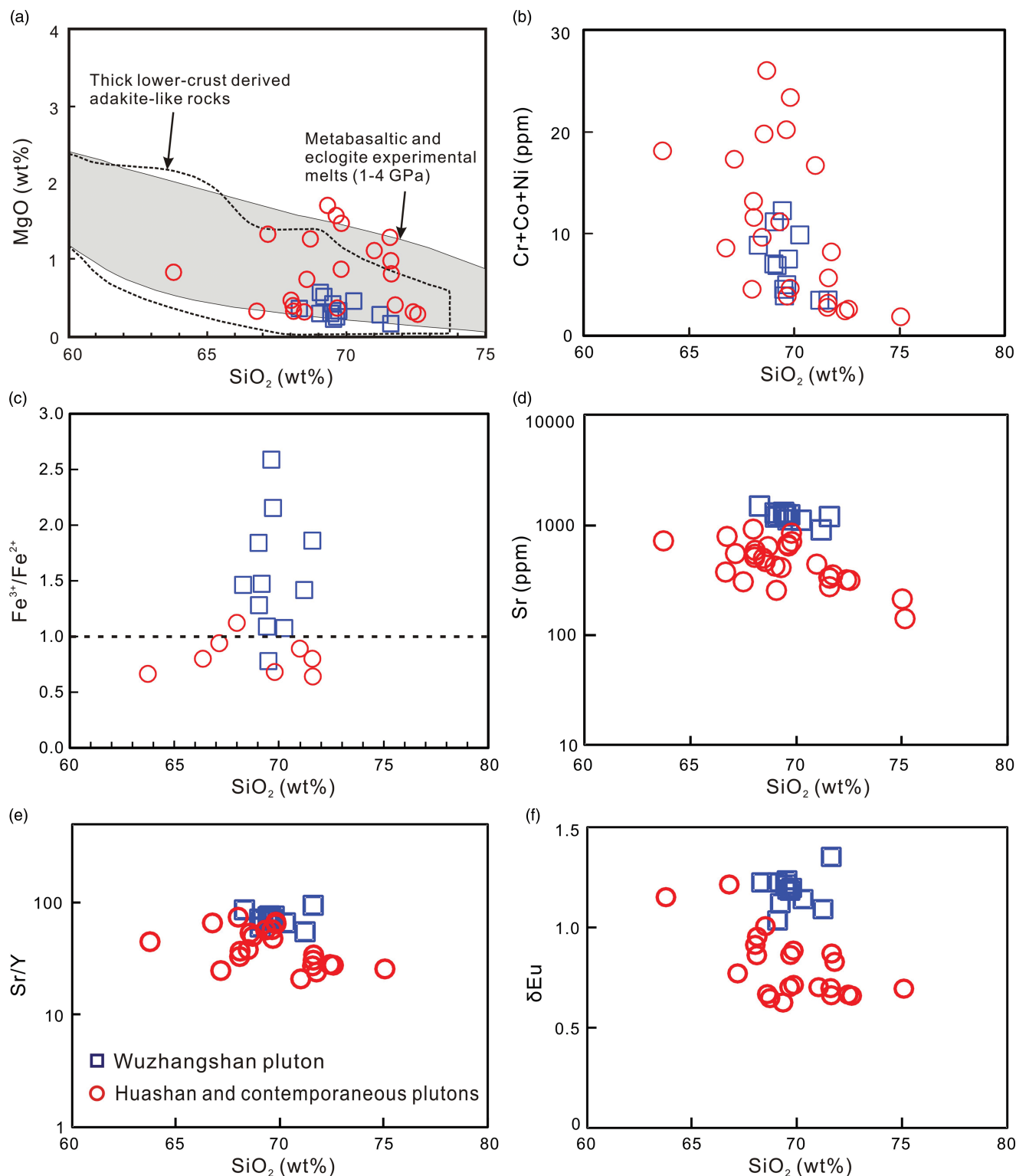


**Fig. 7.** (Colour online) Plots of selected elements and ratios vs  $\text{SiO}_2$  for the Wuzhangshan and Huashan monzogranites. (a) MgO vs  $\text{SiO}_2$ , (b) (Cr + Co + Ni) vs  $\text{SiO}_2$ , (c)  $\text{Fe}^{3+}/\text{Fe}^{2+}$  vs  $\text{SiO}_2$ , (d) Sr vs  $\text{SiO}_2$ , (e) Sr/Y vs  $\text{SiO}_2$  and (f)  $\delta\text{Eu}$  vs  $\text{SiO}_2$ . The field of thick lower crust-derived adakite-like rocks is after Wang *et al.* (2006). The field of metabasaltic and eclogite experimental melts (1–4 GPa) is from the following: Sen & Dunn (1994), Rapp *et al.* (1999, 2002, 2003), Skjerlie & Patino Douce (2002), and references therein. Data of other felsic rocks contemporaneous with Huashan monzogranite in the Xiong'er shan are from Yao *et al.* (2009) and Cao *et al.* (2016).

plutonic rocks show low MgO, Cr, Co and Ni contents, and all samples fall in the field of adakite-like rocks derived from partial melting of thick lower crust and experimental melts of metabasalt

or eclogite at the pressure of 1.0–4.0 GPa in the  $\text{SiO}_2$  vs MgO diagram (Fig. 7a). These features, together with relatively homogeneous elemental and isotopic compositions (Tables 1–4),

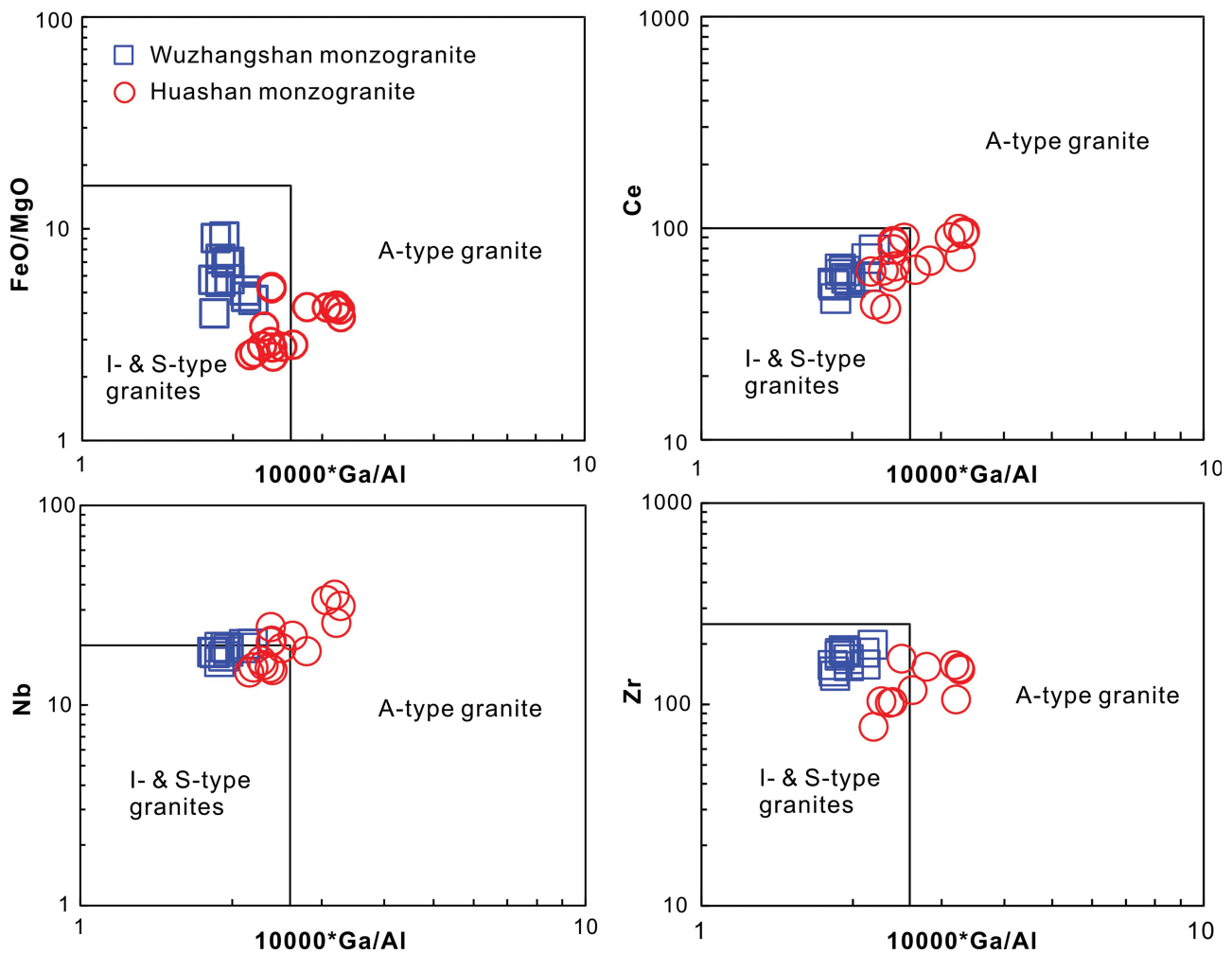


**Fig. 8.** (Colour online)  $\text{FeO}^*/\text{MgO}$ , Ce, Nb and Zr versus  $10000 \cdot \text{Ga}/\text{Al}$  discrimination diagrams of Whalen *et al.* (1987), showing the A-type nature of the Huashan monzogranites in the Xiong'er shan area.

indicate that the Wuzhangshan magma came directly from a thick lower-crust source, e.g. newly underplated basaltic lower crust or ancient basement rocks. The newly underplated basaltic lower crust is not considered to be a potential magma source area for the Wuzhangshan pluton because these rocks have negative  $\epsilon\text{Nd}(t)$  and  $\epsilon\text{Hf}(t)$  values. The oldest basement rocks in the Xiong'er shan area are metamorphosed rocks of the Taihua Group, which formed in the Neoproterozoic to Palaeoproterozoic (2.84–2.26 Ma) and strongly deformed and metamorphosed at 2.1–1.8 Ga (Xu *et al.* 2009; Huang *et al.* 2012). Another widespread ancient rock in the region is volcanic rocks of the Xiong'er Group that formed at 1.80–1.75 Ga (Zhao *et al.* 2004). The two-stage Nd and Hf model ages of the Wuzhangshan monzogranites range from 2646 to 2491 Ma and from 2931 to 2773 Ma (except one spot), respectively, similar to the forming ages of the Taihua Group. The Sr–Nd isotopic compositions of the Wuzhangshan monzogranites are consistent with those of the amphibolites of the Taihua Group, but are obviously different from those of the volcanic rocks of the Xiong'er Group (Fig. 13). On the  $\epsilon\text{Hf}(t)$ –age diagram (Fig. 9), all spots of the Wuzhangshan monzogranites lie in the evolution zone of the Taihua Group amphibolites. Moreover, the CL images and LA-ICP-MS study have identified many

inherited zircon grains in the Wuzhangshan monzogranites. Three of them are analysed in this study, and yield old  $^{207}\text{Pb}/^{206}\text{Pb}$  ages of 2465–1915 Ma with  $\epsilon\text{Hf}(t)$  values of  $-1.8$ , consistent with those of the Taihua Group (Fig. 9). Based on these lines of evidence, we conclude that the Wuzhangshan monzogranites were formed directly from partial melting of the Neoproterozoic to Palaeoproterozoic Taihua Group metamorphic basement rocks, presumably due to heating from a basaltic melt that underplated the continent.

The Huashan and Wuzhangshan monzogranites share many geochemical features, e.g. they are both slightly peraluminous and high-K calcalkalic to shoshonitic rocks, and have adakitic affinities. These features invite speculation that the Huashan monzogranites may also have occurred due to partial melting of the Taihua Group metamorphic basement rocks. Nevertheless, the Huashan monzogranites have a wider range of  $\text{SiO}_2$ , and higher MgO, Cr, Co and Ni, but lower Sr/Y,  $\text{Fe}^{3+}/\text{Fe}^{2+}$  and Sr, relative to the Wuzhangshan monzogranites (Fig. 7), suggesting that these basement rocks cannot be solely responsible for the magma source of the Huashan pluton. Furthermore, two-stage Hf and Nd model ages (1961–1781 Ma and 2268–1549 Ma, respectively) of the Huashan pluton and contemporaneous felsic rocks in the

**Table 3.** LA-ICP-MS *in situ* analysis of zircon Lu–Hf isotopic composition of the Wuzhangshan and Huashan monzogranites in the Xiong'er shan area

Spots	Age	<sup>176</sup> Yb/ <sup>177</sup> Hf		<sup>176</sup> Lu/ <sup>177</sup> Hf		<sup>176</sup> Hf/ <sup>177</sup> Hf		<sup>176</sup> Hf/ <sup>177</sup> Hf(t)	εHf(0)	εHf(t)	TDM1	TDM2
	Ma	Ratio	2σ	Ratio	2σ	Ratio	2σ				Ma	Ma
<i>WZS03 monzogranite of the Wuzhangshan pluton</i>												
WZS03-2	160	0.090882	0.001575	0.002071	0.000026	0.281930	0.000023	0.281924	−30.22	−26.89	1911	2869
WZS03-4	161	0.101208	0.001567	0.002211	0.000035	0.281943	0.000028	0.281936	−29.79	−26.45	1901	2842
WZS03-6	162	0.152204	0.001163	0.003028	0.000021	0.281953	0.000021	0.281943	−29.44	−26.17	1929	2825
WZS03-8	160	0.118103	0.002731	0.002662	0.000050	0.281917	0.000025	0.281909	−30.70	−27.43	1961	2902
WZS03-10	160	0.137700	0.001076	0.002919	0.000019	0.281973	0.000020	0.281964	−28.72	−25.48	1894	2781
WZS03-11	161	0.110338	0.002735	0.002436	0.000049	0.281961	0.000018	0.281954	−29.14	−25.83	1886	2803
WZS03-13	161	0.073566	0.000698	0.001451	0.000005	0.281639	0.000025	0.281634	−40.53	−37.12	2286	3504
WZS03-14	160	0.116784	0.002232	0.002569	0.000031	0.281914	0.000027	0.281906	−30.80	−27.53	1961	2908
WZS03-16	165	0.078451	0.000423	0.001686	0.000005	0.281917	0.000024	0.281912	−30.69	−27.22	1910	2893
WZS03-18	161	0.125605	0.002753	0.002734	0.000053	0.281904	0.000027	0.281896	−31.16	−27.89	1985	2931
WZS03-19	160	0.070582	0.000527	0.001524	0.000008	0.281972	0.000021	0.281967	−28.76	−25.35	1825	2773
Average		0.106857	0.001589	0.002299	0.000027	0.281911	0.000024	0.281904	−31.48	−28.14	1950	2947
<i>WZS03 Inherited zircon</i>												
WZS03-LH02	2465	0.042201	0.000483	0.000786	0.000006	0.281189	0.000021	0.281152	−56.43	−1.79	2857	3093
<i>HS09 monzogranite of the Huashan pluton</i>												
HS09-01	130	0.026728	0.000218	0.000915	0.000004	0.282397	0.000016	0.282394	−13.73	−10.92	1206	1846
HS09-02	128	0.025812	0.000351	0.000984	0.000010	0.282381	0.000019	0.282379	−14.29	−11.53	1230	1883
HS09-03	127	0.021430	0.000285	0.000874	0.000006	0.282364	0.000018	0.282362	−14.88	−12.13	1249	1920
HS09-04	124	0.030709	0.000099	0.001068	0.000002	0.282414	0.000016	0.282411	−13.12	−10.45	1186	1812
HS09-05	128	0.027924	0.000159	0.000953	0.000003	0.282426	0.000016	0.282424	−12.68	−9.91	1165	1781
HS09-06	127	0.021641	0.000072	0.000894	0.000003	0.282355	0.000016	0.282353	−15.21	−12.48	1263	1941
HS09-07	126	0.020401	0.000137	0.000757	0.000003	0.282389	0.000015	0.282388	−13.99	−11.26	1211	1864
HS09-08	131	0.028921	0.000145	0.001004	0.000004	0.282415	0.000017	0.282412	−13.09	−10.27	1183	1806
HS09-09	127	0.016621	0.000402	0.000660	0.000012	0.282345	0.000015	0.282344	−15.55	−12.79	1269	1961
Average		0.024465	0.000207	0.000901	0.000005	0.282387	0.000016	0.282385	−14.07	−11.31	1218	1869

Xiong'er shan and its adjacent areas are much younger than the Taihua Group. The Huashan monzogranites and contemporaneous felsic rocks have higher  $\epsilon\text{Nd}(t)$  and  $\epsilon\text{Hf}(t)$  values than those of the Taihua Group, and all the samples plot in the area between the Taihua Group amphibolite rocks and the 122 Ma diorite that was derived from a relatively juvenile mantle source (Gao *et al.* 2014) in the age vs  $\epsilon\text{Hf}(t)$  and  $(^{87}\text{Sr}/^{86}\text{Sr})_t$  vs  $\epsilon\text{Nd}(t)$  diagrams (Figs 9 and 12). These geochemical data indicate that the mantle-derived magmas with depleted Nd and Hf isotopic composition must have been involved in the petrogenesis of the Huashan monzogranites. Generally, the crust-derived granite containing mantle component in non-arc setting is believed to come from mixing of mantle- and crust-derived melts (e.g. Griffin *et al.* 2002; Barbarin, 2005) or the partial melting of delaminated lower crust (e.g. Rapp *et al.* 1999; Wang *et al.* 2006). Many samples of the Huashan pluton have a lower Sr content and Sr/Y ratio than those of the Wuzhangshan pluton (Figs 4d, 7d, e, f), and show negative Sr and Eu anomalies (Figs 5, 6), suggesting that the Huashan

monzogranites were probably not generated by partial melting of delaminated lower crust. However, mafic microgranular enclaves with ellipsoidal to spherical shapes are enclosed within the Huashan pluton (Nie *et al.* 2015), which has been generally interpreted as evidence of mixing between mafic and felsic magmas (e.g. Perugini *et al.* 2003; Barbarin, 2005). Moreover, sporadic mafic magmatic rocks in the Xiong'er shan and its adjacent areas have been reported in the last decade (Gao & Zhao, 2017). The mafic magmatic rocks which have zircon U–Pb ages of 148–117 Ma, with peak ages of 129–117 Ma (Xie *et al.* 2007; Bao *et al.* 2009; Gao *et al.* 2014), are contemporary with the Huashan monzogranites, indicating that crust–mantle interaction likely occurred in this region. High  $\text{SiO}_2$  samples of the Huashan pluton have more evolved isotopic compositions (Fig. 12), indicative of the mixing between a mafic melt and a crustal component (Van der Meer *et al.* 2018). The above evidence, together with elemental and isotopic composition and model ages, suggests that the Huashan monzogranites were probably generated by mixing of mantle-derived magmas

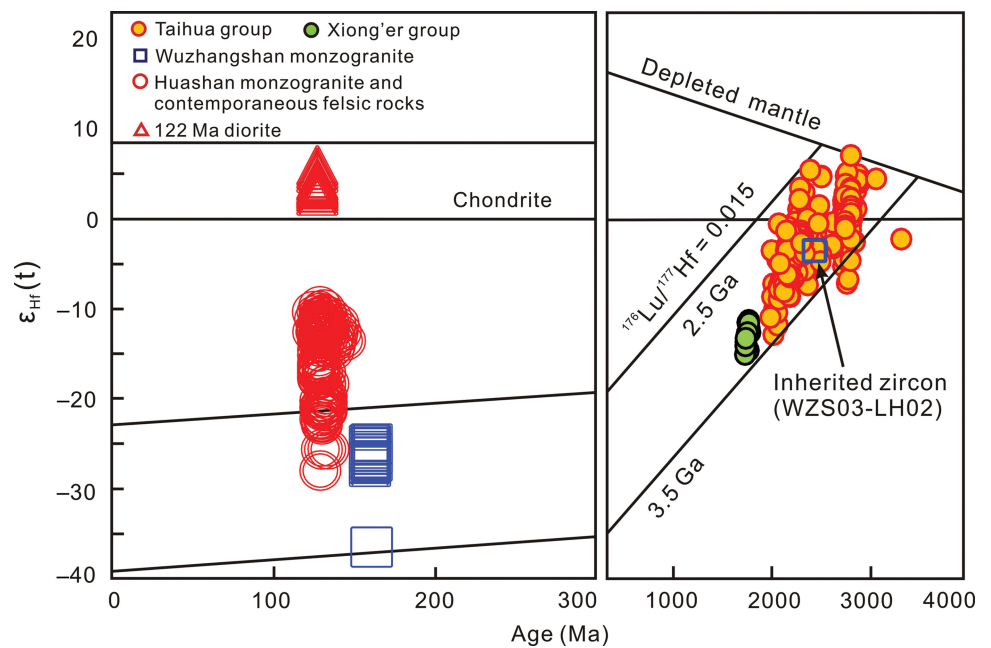


**Fig. 9.** (Colour online) Variation of initial  $\epsilon_{\text{Hf}}(t)$  isotope values vs the zircon U–Pb ages of the Wuzhangshan and Huashan plutons in the Xiong’ershan area. Data for the Taihua Group are from Liu *et al.* (2009), Xu *et al.* (2009), Diwu *et al.* (2010) and Huang *et al.* (2012). Data for the Xiong’er Group are from Wang *et al.* (2010). Data for 122 Ma diorite and the felsic rocks contemporaneous with Huashan monzogranite in the Xiong’ershan area are from Yao *et al.* (2009), Xiao *et al.* (2012), Gao *et al.* (2014) and Cao *et al.* (2016).

**Table 4.** Whole-rock Sr–Nd isotopic compositions of the Wuzhangshan monzogranites in the Xiong’ershan area

Samples	Rb	Sr	$^{87}\text{Rb}/^{86}\text{Sr}$	$^{87}\text{Sr}/^{86}\text{Sr}$	$2\sigma$	$(^{87}\text{Sr}/^{86}\text{Sr})_t$	Sm	Nd	$^{147}\text{Sm}/^{144}\text{Nd}$	$^{143}\text{Nd}/^{144}\text{Nd}$	$2\sigma$	$(^{143}\text{Nd}/^{144}\text{Nd})_t$	$\epsilon_{\text{Nd}}(t)$	$T_{\text{DM2}}(\text{Ma})$
WZS01	142	1212	0.339183	0.708009	0.000008	0.707237	3.97	26.0	0.092303	0.511479	0.000006	0.511382	–20.49	2609
WZS02	137	1303	0.304386	0.708043	0.000013	0.707351	3.74	22.3	0.101383	0.511551	0.000006	0.511445	–19.27	2509
WZS03	144	1238	0.336737	0.707868	0.000009	0.707102	3.88	23.5	0.099807	0.511494	0.000006	0.511390	–20.35	2596
WZS04	135	1487	0.262828	0.707863	0.000013	0.707265	3.69	21.9	0.101854	0.511513	0.000005	0.511406	–20.02	2569
WZS05	114	1115	0.295991	0.708137	0.000010	0.707464	3.75	22.4	0.101200	0.511562	0.000009	0.511456	–19.05	2491
WZS06	143	1287	0.321667	0.708156	0.000017	0.707424	3.93	23.6	0.100665	0.511525	0.000009	0.511420	–19.76	2549
WZS07	133	1211	0.317948	0.708327	0.000008	0.707604	3.43	20.7	0.100166	0.511463	0.000006	0.511358	–20.96	2646
WZS08	142	904	0.454746	0.708638	0.000013	0.707604	3.38	21.0	0.097296	0.511498	0.000007	0.511396	–20.22	2586
WZS09	144	1247	0.334306	0.708235	0.000011	0.707475	3.90	23.8	0.099057	0.511478	0.000009	0.511374	–20.64	2620
WZS10	152	1193	0.368852	0.707662	0.000016	0.706823	2.62	17.3	0.091549	0.511545	0.000008	0.511449	–19.18	2504

and melts generated through the reworking of the Taihua Group metamorphic basement rocks.

### 7.c. Implication for gold mineralization in the Xiong’ershan area

The gold deposits in the Xiong’ershan area, the third largest gold concentration in China (Mao *et al.* 2002), have been extensively studied in recent decades (e.g. Mao *et al.* 2002; Chen *et al.* 2008; Tang *et al.* 2013; Tang, 2014; Tian *et al.* 2017), but their origins remain debated and not well understood. Several contrasting genetic models have been proposed, including (1) the gold deposits are considered as greenstone type (Li *et al.* 1996), assigning the metamorphic rocks as the source for the metallic ores (Li & Santosh, 2017); (2) they are orogenic gold deposits formed during the Mesozoic continental collision regime, suggesting the ore-forming materials derived from the Taihua Group metamorphic

rocks and/or late Mesozoic magmatic rocks (e.g. Goldfarb *et al.* 1998; Mao *et al.* 2002; Chen *et al.* 2008); and (3) a late Mesozoic magma-related hydrothermal origin (e.g. Yao *et al.* 2009; Zhai *et al.* 2011; Tang *et al.* 2013; Tian *et al.* 2017). The focuses of the debate are on the source of ore-forming materials, and the key factor controlling the formation of gold deposits in the Xiong’ershan area: the ancient metamorphic basement (e.g. Taihua Group) or late Mesozoic magmatism?

In fact, there is almost a two-billion-year time gap between metamorphism and gold mineralization in the Xiong’ershan area (Li & Santosh, 2017); and the tectonic environment, metamorphic setting and mineralogical characteristics of the gold deposits are different from the accepted models of global orogenic gold deposits (Groves *et al.* 1998). Conversely, the gold deposits in the Xiong’ershan area are mainly distributed around the Huashan and Heyu plutons (Mao *et al.* 2002) and several small granite stocks (Fig. 1c), and their mineralogical characteristics and fluid



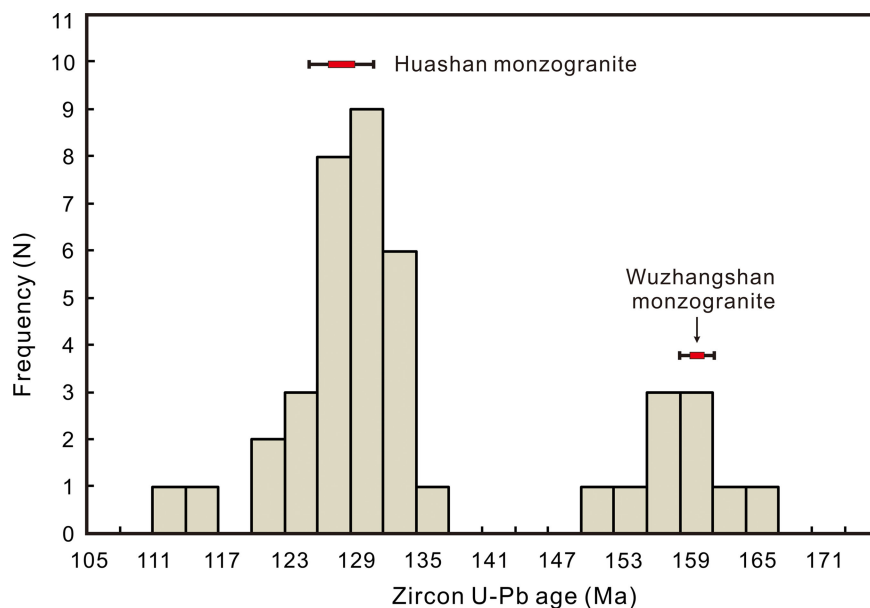


**Fig. 10.** (Colour online) Zircon U-Pb age histograms of the Late Jurassic to Early Cretaceous magmatic rocks in the Xiong'er shan area. Data source same as Table S1 (in Supplementary Material at <https://doi.org/10.1017/S0016756819000888>).

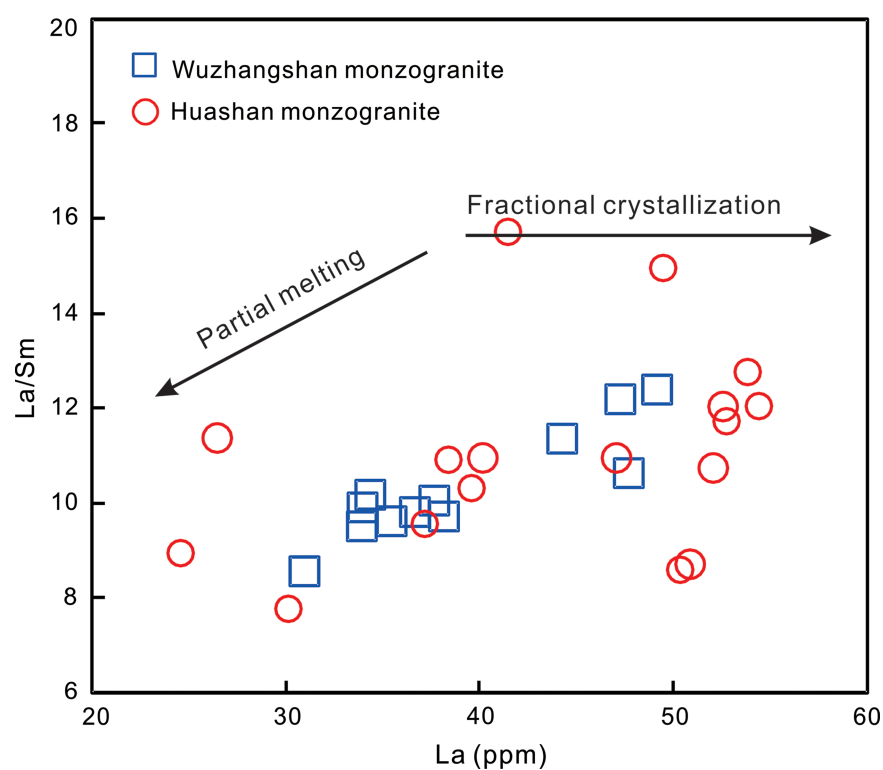


**Fig. 11.** (Colour online) La/Y vs La diagram for the Wuzhangshan and Huashan plutons in the Xiong'er shan area.

geochemistry are consistent with those of the magma-related hydrothermal gold deposits (e.g. Yao *et al.* 2009; Zhai *et al.* 2011; Tang *et al.* 2013; Tian *et al.* 2017). Moreover, the sulphur, lead, hydrogen and oxygen isotope data of the gold deposits in the Xiong'er shan area favour a possible magmatic derivation for the gold ores (e.g. Tang *et al.* 2013; Tang, 2014; Tian *et al.* 2017; Li *et al.* 2018). Consequently, most researchers accept that no matter what kind of ore genesis, the gold mineralization in the

Xiong'er shan area has a close connection with late Mesozoic magmatism.

Identification of two magmatic episodes during the Late Jurassic to Early Cretaceous in the Xiong'er shan area, combined with recent reported high-precision chronological data for the timing of mineralization and associated alteration and magmatic rocks, enable us to further explore the link between gold mineralization and late Mesozoic magmatism. Previous Re-Os and  $^{40}\text{Ar}/^{39}\text{Ar}$

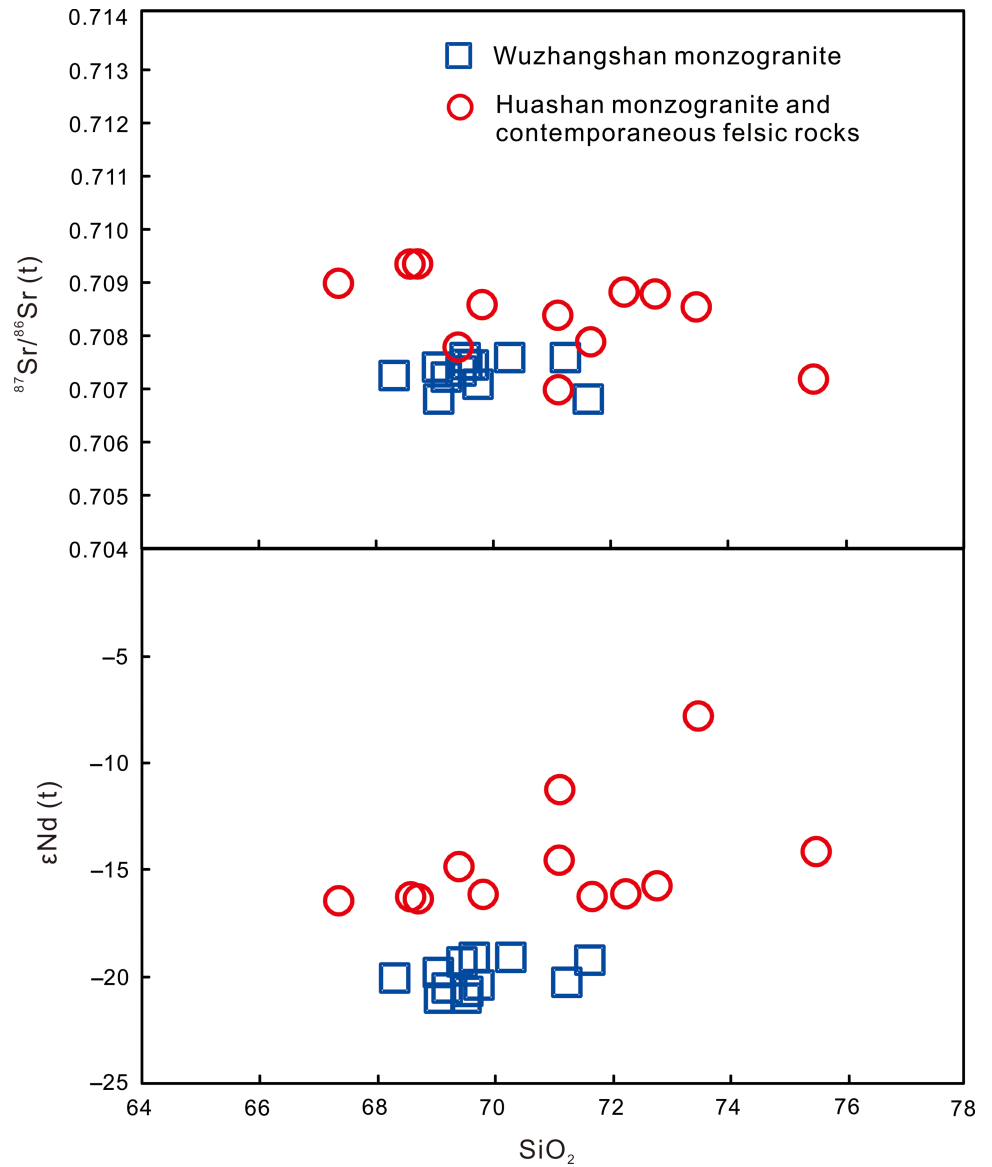


**Fig. 12.** (Colour online) Sr and Nd isotopic compositions vs silica content of the Wuzhangshan and Huashan plutons in the Xiong'er shan area. Data for the felsic rocks contemporaneous with Huashan monzogranite in the Xiong'er shan area are from Gao et al. (2010, 2014) and Cao et al. (2016).

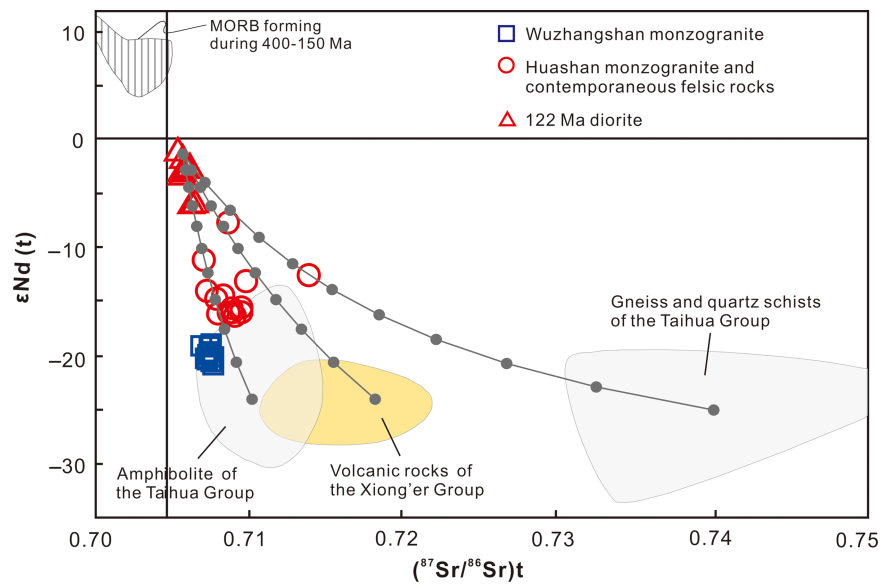


**Fig. 13.** (Colour online) Sr-Nd isotope compositions of the Wuzhangshan and Huashan plutons in the Xiong'er shan area. The data of 400–150 Ma mid-ocean ridge basalt (MORB) are from Wang et al. (2006). Fields of amphibolites of the Taihua Group, gneiss and quartz schists of the Taihua Group, and the volcanic rocks of the Xiong'er Group are after Gao & Zhao (2017). Data for 122 Ma diorite and the felsic rocks contemporaneous with Huashan monzogranite in the Xiong'er shan area are from Gao et al. (2010, 2014) and Cao et al. (2016).

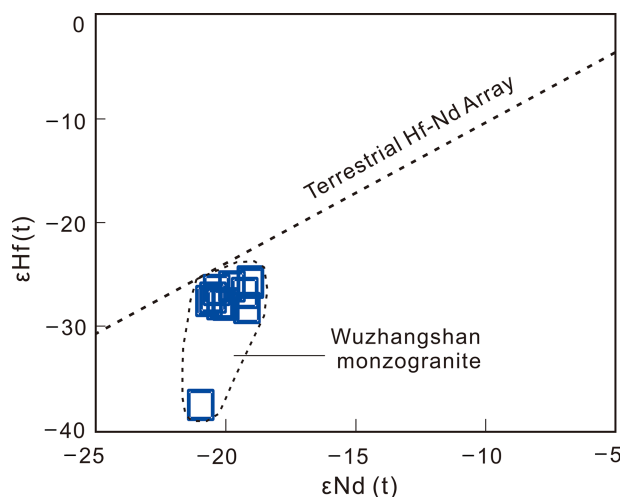


Fig. 14. (Colour online)  $\epsilon\text{Hf}(t)$  vs  $\epsilon\text{Nd}(t)$  diagram of the Wuzhangshan monzogranite. The terrestrial Hf-Nd array after Vervoort *et al.* (2000).

dating indicates that the Qianhe, Miaoling, Qiyugou and Gongyu gold deposits formed between 135 and 115 Ma (Yao *et al.* 2009; Zhai *et al.* 2011; Tang *et al.* 2013; Tang, 2014). More recently, Deng *et al.* (2014) and Cao *et al.* (2017) provided a comprehensive geochronological study of major gold deposits in the Xiong'er shan area, bracketing their formation mainly in the range of 136–110 Ma except for a few Triassic gold deposits (e.g. Shangong and Yaogou). These ages are reasonably consistent with the ages of the late-episode (138–113 Ma) magmatic rocks, indicating the gold mineralization was contemporaneous with emplacement of the late-episode magmas during the Late Jurassic to Early Cretaceous in the Xiong'er shan area. The data presented in this study suggest that the early-episode intrusions were formed directly from partial melting of the Neoproterozoic Taihua Group metamorphic basement rocks, whereas the late-episode intrusions were produced by mixing of crustal- and mantle-derived magmas. Therefore, the gold mineralization coeval with the emplacement of the late-episode magmas implies that crustal–mantle mixed magma might be a better target for gold mineralization compared to the ancient metamorphic basement melt. This invites a reasonable speculation that injection of mantle-derived magmas into a felsic magma chamber is likely to be a key factor controlling the formation of gold deposits in the Xiong'er shan area. The contribution of mantle components to the ore-forming materials was also indicated by mineralogical characteristics and isotope composition of the gold deposits in this region. For example, many deposits (e.g. the Qiyugou, Huanxiangwo gold deposits) in the Xiong'er shan area comprise several telluride, selenide and stibnite minerals (Li & Santosh, 2017). Because of the affinity of Te with refractory (mafic) materials (Salters & Stracke, 2004), the coexistence of Te and Au in the gold deposits is considered as an indication for mantle (Li & Santosh, 2017). The Sr isotopic compositions of sulphides in the Dianfang gold deposit are higher than the value of mantle but lower than that of continental crust, suggesting the metals in this deposit may have been derived from the mixture of crustal and mantle materials (Tian *et al.* 2017). The Pb isotopic results from the Dianfang and Luyuangou gold deposits also display a mixed signature from the mantle and lower crust (Tian *et al.* 2017; Li *et al.* 2018). The Re–Os and He–Ar isotopes from the pyrite of the gold systems in this region provide further evidence that at least

a part of the ore-forming fluids was from the mantle (e.g. Yao *et al.* 2009; Tang, 2014). Additionally, Li & Santosh (2017) found that the gold ore districts (including the Xiong'er shan area) in the southern margin of the NCC are all located at the centres of high heat flow fields that are mainly controlled by the upwelling asthenosphere, reflecting the close relationship between mantle upwelling and gold mineralization.

In summary, all the mineralogical, chronological and isotopic data from igneous rocks and ore minerals suggest that the mantle source plays a crucial role in the gold mineralization of the Xiong'er shan area, although ore-forming components are hypothesized to have multiple sources.

#### 7.d. Implications for the geodynamics

The continental collision between the North China Craton and the Yangtze Craton in the Qinling Orogenic Belt occurred during the early Mesozoic (c. 250–210 Ma), resulting in the lithosphere being markedly compressed, shortened and thickened (Zhang *et al.* 1996). During the late Mesozoic, the tectonic systems of the Qinling Orogenic Belt were shifted from a palaeo-Tethys regime to a palaeo-Pacific regime (Mao *et al.* 2010). At this time, the NCC was undergoing craton destruction and lithospheric thinning (e.g. Lapiere *et al.* 1997; Mao *et al.* 2002, 2010; Windley *et al.* 2010; Gao & Zhao, 2017). Therefore, it has been widely accepted that the Late Jurassic to Early Cretaceous magmatism in the southern margin of the NCC is related to the lithospheric thinning (e.g. Mao *et al.* 2010; Zhao *et al.* 2012; Gao *et al.* 2014). However, previous age estimates for this event vary widely and are not consistent. Gao *et al.* (2004) and Tian *et al.* (2017) suggested the lithospheric delamination and thinning in the southern margin of the NCC were initiated by the Late Jurassic (159–146 Ma). Gao *et al.* (2010, 2014) and Li *et al.* (2012) considered that the transformation of the lithosphere from thickening to thinning in the southern margin of the NCC occurred during 148–135 Ma. Other researchers conclude that intensive removal of the thickened lower crust occurred during the Early Cretaceous, such as 130–126 Ma (Hou *et al.* 2007), 135–108 Ma (Mao *et al.* 2010), and after 130 Ma (Zhao *et al.* 2012) or 127 Ma (Gao & Zhao, 2017).

The Wuzhangshan and Huashan monzogranites preserve the imprints of the two magmatic episodes during the Late Jurassic to Early Cretaceous in the Xiong'er shan area, respectively. Thus, the two monzogranites can be used to estimate the tectonic evolution of the southern margin of the NCC, especially the timing of lithospheric thinning. The Wuzhangshan monzogranites exhibit typical geochemical features of adakites, and are formed from partial melting of the Taihua Group metamorphic basement rocks. The flat patterns in heavy REEs with  $\text{Y}/\text{Yb} = 7.6\text{--}8.9$  and  $(\text{Dy}/\text{Yb})_{\text{N}} = 0.8\text{--}1.0$ , indicate that the amphibole should be the most important residual mineral in the Wuzhangshan monzogranite source because garnet is strongly compatible for HREEs but the amphibole is compatible for MREEs and Y (Defant & Drummond, 1990; Du *et al.* 2018). Generally, garnet is preferential retention of Lu over Hf, and thus, the presence of garnet in a restite could trigger decoupling of Hf–Nd evolution (Vervoort *et al.* 2000). The Wuzhangshan monzogranites show  $\epsilon\text{Hf}(t)$  and  $\epsilon\text{Nd}(t)$  mean values of  $-28.1$  and  $-20.0$ , and display slight diversion from the terrestrial Hf–Nd array (Fig. 14), suggesting that their source also contains minor residual garnet. Additionally, plagioclase is inferred to be not a residual phase in the source region, as indicated by the negligible to slightly positive Eu anomalies (Table 2; Fig. 6) and obviously positive Sr anomalies (Fig. 5) of

the Wuzhangshan monzogranites. Experimental studies (e.g. Sen & Dunn, 1994; Rapp *et al.* 1999, 2002, 2003) indicate that when mafic rocks are partially melted, garnet becomes stable at pressures equivalent to crustal thickness of >40–50 km (~1.2–1.5 GPa); plagioclase becomes unstable at depths greater than *c.* 50 km (1.5 GPa). Therefore, the residual phases include amphibole and minor garnet but no plagioclase, indicating the crustal thickness in the Xiong'er shan area must have been at least 50 km when the Wuzhangshan monzogranites were formed. This is consistent with crustal thickness estimation from the Mesozoic lower crust mafic xenoliths (~160 Ma) in Xinyang, southern margin of the NCC (Zheng *et al.* 2003).

Geochemical characteristics of the Huashan monzogranites, such as enrichment of LREE and flat HREE patterns, negative Eu anomalies and the depletion in Sr with low Sr/Y ratio (Figs 4d, 5, 6), indicate that their parental magmas were generated under lower pressure than that of the Wuzhangshan monzogranites, and amphibole and plagioclase were important residual phases in the source region (e.g. Martin *et al.* 2005). Consequently, the crustal thickness in the Xiong'er shan area must have been less than 40 km when the Huashan monzogranites were formed. This is also consistent with the results of other studies. Based on the xenoliths studies, Zheng *et al.* (2003) suggested that the Cenozoic lithosphere was significantly thinner than the Mesozoic, and up to 10 km of lowermost crust was delaminated. Several other studies show that the present crust thickness in the Xiong'er shan area is only ~35 km (Sun & Toksoz, 2006), and less than 5 km thickness of the upper crust has been eroded since the Early Cretaceous (Zhao *et al.* 2012). Therefore, the continental crust in the Xiong'er shan area must have undergone some thinning after the formation of the Wuzhangshan monzogranites (~160 Ma) but before the emplacement of the Huashan monzogranites (~127 Ma). This further indicates that the gold metallogenic and late-episode magmatic activities occurring during the Late Mesozoic in the Xiong'er shan area were probably associated with the lithospheric thinning.

More than half of the samples from the Huashan monzogranites exhibit geochemical characteristics of A-type granites (Fig. 8). The emplacement of the Huashan A-type granites is coeval with the exhumation of metamorphic core complexes and the formation of several deformed basins (Xie *et al.* 2007; Mao *et al.* 2010), indicative of lithospheric extension that dominated the southern margin of the NCC during the emplacement of the Huashan magmas. This, in combination with the lack of magmatic rocks derived from the delaminated lower crust, implies that the crustal thinning during the late Mesozoic in the Xiong'er shan area may be caused by the lithospheric extension, similar to that of SE China (Wang *et al.* 2004).

As discussed above, the evolution from the Wuzhangshan to Huashan monzogranites marks a change of tectonic regime into an extensional setting, and the lithosphere transformed from thickening to thinning in the Xiong'er shan area, southern margin of the NCC. Lithospheric thinning triggered asthenospheric upwelling, mafic magma underplating, partial melting of the lower crust, and crust–mantle magma mixing. The underplated mantle-derived basaltic magmas supplied both energy and materials for the formation of the late-episode magmatic rocks and gold deposits in the Xiong'er shan area.

## 8. Conclusions

- (1) Two episodes of magmatism (165–150 Ma and 138–113 Ma) are recognized in the Xiong'er shan area. Zircon LA-ICP-MS

U–Pb dating for the Wuzhangshan and Huashan monzogranites yields ages of  $160.7 \pm 0.6$  Ma and  $127.2 \pm 1.0$  Ma, respectively, representing the two magmatic episodes.

- (2) The Wuzhangshan monzogranites were derived directly from partial melting of the Neoarchaean to Palaeoproterozoic Taihua Group metamorphic basement rocks (especially the mafic amphibolites), whereas the Huashan monzogranites were probably generated by mixing of mantle-derived magmas and melts generated through the reworking of the Taihua Group metamorphic basement rocks.
- (3) All the mineralogical, chronological and isotopic data from igneous rocks and ore minerals suggest that the mantle source plays a crucial role in the gold mineralization of the Xiong'er shan area.
- (4) The gold metallogenic and late-episode magmatic activities during the Late Jurassic to Early Cretaceous in the Xiong'er shan area were probably related to the lithospheric thinning. The transformation of the lithosphere from thickening to thinning in the Xiong'er shan area, southern margin of the NCC probably occurred between ~160 Ma and ~127 Ma, and was witnessed by the evolution from the Wuzhangshan to Huashan monzogranites.

**Acknowledgements.** This study was supported financially by the National Natural Science Foundation of China (grant no. 41403032, 41202050) and the China Geological Survey (grant no. 12120113083000). Senior Engineers Weizhi Sun and Jianhui Xiao, and Master Students Xiaowei Zhang, Shaolei Kou and Hongxiang Jia provided valuable assistance in the field and laboratory.

**Declaration of Interest.** None.

**Supplementary material.** To view supplementary material for this article, please visit <https://doi.org/10.1017/S0016756819000888>

## References

- Anderson T (2002) Correction of common lead in U–Pb analyses that do not report  $^{204}\text{Pb}$ . *Chemical Geology* **192**, 59–79.
- Andrade S, Hypolito R, Ulbrich HHGJ and Silva ML (2002) Iron II oxide determination in rocks and minerals. *Chemical Geology* **182**, 85–9.
- Bao ZW, Li CJ and Qi JP (2009) SHRIMP zircon U–Pb age of the gabbro dyke in the Luanchuan Pb–Zn–Ag orefield, east Qinling orogen and its constraint on mineralization time. *Acta Petrologica Sinica* **25**, 2951–6.
- Bao ZW, Sun WD, Zartman RE, Yao JM and Gao, XY (2017) Recycling of subducted upper continental crust: constraints on the extensive molybdenum mineralization in the Qinling–Dabie orogen. *Ore Geology Reviews* **81**, 451–65.
- Bao ZW, Wang CY, Zhao TP, Li CJ and Gao XY (2014) Petrogenesis of the Mesozoic granites and Mo mineralization of the Luanchuan ore field in the East Qinling Mo mineralization belt, Central China. *Ore Geology Reviews* **57**, 132–53.
- Barbarin B (2005) Mafic magmatic enclaves and mafic rocks associated with some granitoids of the central Sierra Nevada batholith, California: nature, origin, and relations with the hosts. *Lithos* **80**, 155–77.
- Bouvier A, Vervoort JD and Patchett PJ (2008) The Lu–Hf and Sm–Nd isotopic composition of CHUR: constraints from unequilibrated chondrites and implications for the bulk composition of terrestrial planets. *Earth and Planetary Science Letters* **273**, 48–57.
- Cao J, Ye HS, Chen XD, Li ZY, Zhang XK and He W (2016) Geochronology, geochemistry and Sr–Nd–Hf isotopic compositions of granite porphyry in Leimengou Mo deposit, western Henan Province. *Mineral Deposits* **35**, 677–95 (in Chinese with English abstract).
- Cao MP, Yao JM, Deng XH, Yang FJ, Mao GZ and Mathur R (2017) Diverse and multistage Mo, Au, Ag–Pb–Zn and Cu deposits in the Xiong'er Terrane, East Qinling: from Triassic Cu mineralization. *Ore Geology Reviews* **81**, 565–74.

- Castillo PR, Janney PE and Solidum RU (1999) Petrology and geochemistry of Camiguin Island, southern Philippines: insights to the source of adakites and other lavas in a complex arc setting. *Contributions to Mineralogy and Petrology* **134**, 33–51.
- Chen YJ, Pirajno F and Qi JP (2008) The Shanggong gold deposit, Eastern Qinling Orogen, China: isotope geochemistry and implications for ore genesis. *Journal of Asian Earth Sciences* **33**, 252–66.
- Chu NC, Taylor RN, Chavagnac V, Nesbitt RW, Boella RM, Milton JA, German CR, Bayon G and Burton K (2002) Hf isotope ratio analysis using multi-collector inductively coupled plasma mass spectrometry: an evaluation of isobaric interference corrections. *Journal of Analytical Atomic Spectrometry* **17**, 1567–74.
- Defant MJ and Drummond MS (1990) Derivation of some modern arc magmas by melting of young subducted lithosphere. *Nature* **347**, 662–5.
- Deng J, Gong Q, Wang C, Carranza EJM and Santosh M (2014) Sequence of Late Jurassic–Early Cretaceous magmatic–hydrothermal events in the Xiong'er shan region, Central China: an overview with new zircon U–Pb geochronology data on quartz porphyries. *Journal of Asian Earth Sciences* **79**, 161–72.
- Diwu CR, Sun Y, Lin CL and Wang HL (2010) LA–(MC)–ICPMS U–Pb zircon geochronology and Lu–Hf isotope compositions of the Taihua complex on the southern margin of the North China Craton. *Chinese Science Bulletin* **55**, 2557–71.
- Dong YP and Santosh M (2016) Tectonic architecture and multiple orogeny of the Qinling Orogenic Belt, Central China. *Gondwana Research* **29**, 1–40.
- Du JG, Du YS and Cao Y (2018) Important role of hornblende fractionation in generating the adakitic magmas in Tongling, Eastern China: evidence from amphibole megacryst and cumulate xenoliths and host gabbros. *International Geology Review*, **60**, 1381–403.
- Gao S, Rudnick RL, Yuan HL, Liu XM, Liu YS, Xu WL, Ling WL, Ayers J, Wang XC and Wang QH (2004) Recycling lower continental crust in the North China Craton. *Nature* **432**, 892–7.
- Gao XY and Zhao TP (2017) Late Mesozoic magmatism and tectonic evolution in the Southern margin of the North China Craton. *Science in China Series D: Earth Sciences* **60**, 1959–75.
- Gao XY, Zhao TP, Bao ZW and Yang AY (2014) Petrogenesis of the early Cretaceous intermediate and felsic intrusions at the southern margin of the North China Craton: implications for crust–mantle interaction. *Lithos* **206–207**, 65–78.
- Gao XY, Zhao TP, Yuan ZL, Zhou YY and Gao JF (2010) Geochemistry and petrogenesis of the Heyu batholith in the southern margin of the North China block. *Acta Petrologica Sinica* **26**, 3485–506.
- Goldfarb RJ, Phillips GN and Nokleberg WJ (1998) Tectonic setting of syn-orogenic gold deposits of the Pacific Rim. *Ore Geology Reviews* **13**, 185–218.
- Griffin WL, Pearson NJ, Belousova E, Jackson SE, Van Acherbergh E, O'Reilly SY and Shee SR (2000) The Hf isotope composition of cratonic mantle: LAM–MC–ICP MS analysis of zircon megacrysts in kimberlites. *Geochimica et Cosmochimica Acta* **64**, 133–47.
- Griffin WL, Wang X, Jackson SE, Pearson NJ, O'Reilly SY, Xu X and Zhou X (2002) Zircon chemistry and magma mixing, SE China: in-situ analysis of Hf isotopes, Tonglu and Pingtan igneous complexes. *Lithos* **61**, 237–69.
- Groves DI, Goldfarb RJ, Gebre-Mariam M, Hagemann SG and Robert F (1998) Orogenic gold deposits: a proposed classification in the context of their crustal distribution and relationship to other gold deposit types. *Ore Geology Reviews* **13**, 7–27.
- Han YG, Zhang SH, Franco P and Zhang YH (2007) Evolution of the Mesozoic granites in the Xiong'er shan–Waifangshan region, western Henan Province, China, and its tectonic implications. *Acta Geologica Sinica* **81**, 253–265.
- He YH, Zhao GC, Sun M and Han YG (2010) Petrogenesis and tectonic setting of volcanic rocks in the Xiaoshan and Waifangshan areas along the southern margin of the North China Craton: constraints from bulk-rock geochemistry and Sr–Nd isotopic composition. *Lithos* **114**, 186–99.
- Hou KJ, Li YH and Tian YR (2009) In situ U–Pb zircon dating using laser ablation–multi ion counting–ICP–MS. *Mineral Deposits* **28**, 481–92 (in Chinese with English abstract).
- Hou ML, Jiang YH, Jiang SY, Ling HF and Zhao KD (2007) Contrasting origins of late Mesozoic adakitic granitoids from the northwestern Jiaodong Peninsula, east China: implications for crustal thickening to delamination. *Geological Magazine* **144**, 619–31.
- Huang XL, Wilde SA, Yang QJ and Zhong JW (2012) Geochronology and petrogenesis of gray gneisses from the Taihua Complex at Xiong'er in the southern segment of the trans-North China orogen: implications for tectonic transformation in the early Paleoproterozoic. *Lithos* **134–135**, 236–52.
- Jackson SE, Pearson NJ, Griffin WL and Belousova EA (2004) The application of laser ablation–inductively coupled plasma–mass spectrometry to in situ U–Pb zircon geochronology. *Chemical Geology* **211**, 47–69.
- Jacobsen SB and Wasserburg GJ (1980) Sm–Nd isotopic evolution of chondrites. *Earth and Planetary Science Letters* **50**, 139–55.
- Kuritani T, Kimura JI, Miyamoto T, Wei HQ and Shimano T (2009) Intraplate magmatism related to deceleration of upwelling asthenospheric mantle: implications from the Changbaishan shield basalts, northeast China. *Lithos* **112**, 247–58.
- Kuritani T, Sakuyama T, Kamada N, Yokoyama T and Nakagawa M (2017) Fluid-fluxed melting of mantle versus decompression melting of hydrous mantle plume as the cause of intraplate magmatism over a stagnant slab: implications from Fukue Volcano Group, SW Japan. *Lithos* **282–283**, 98–110.
- Lapierre H, Jahn BM, Charvet J and Yu YW (1997) Mesozoic felsic arc magmatism and continental olivine tholeiites in Zhejiang Province and their relationship with the tectonic activity in southeastern China. *Tectonophysics* **274**, 321–38.
- Li N, Chen YJ, Pirajno F, Gong HJ, Mao SD and Ni ZY (2012) LA–ICP–MS zircon U–Pb dating, trace element and Hf isotope geochemistry of the Heyu granite batholith, eastern Qinling, central China: implications for Mesozoic tectono–magmatic evolution. *Lithos* **142–143**, 34–47.
- Li SM, Qu LQ, Su ZB, Huang JJ, Wang XS and Yue ZS (1996) *The Geology and Metallogenic Prediction of the Gold Deposit in Xiaolinling*. Beijing: Geological Publishing House, 250 pp. (in Chinese).
- Li SR and Santosh M (2017) Geodynamics of heterogeneous gold mineralization in the North China Craton and its relationship to lithospheric destruction. *Gondwana Research* **50**, 267–92.
- Li W, Zhao T, Zhang Y and Tao N (2018) Field geology, geochronology, and isotope geochemistry of the Luyuangou gold deposit, China: implications for the gold mineralization in the eastern Qinling Orogen. *Geological Journal* **53**, 96–112.
- Liew TC and Hofmann AW (1988) Precambrian crustal components, plutonic associations, plate environment of the Hercynian Fold Belt of central Europe: indications from a Nd and Sr isotopic study. *Contributions to Mineralogy and Petrology* **98**, 129–38.
- Liu DY, Wilde SA, Wan YS, Wang SY, Valley JW, Kita N, Dong CY, Xie HQ, Yang CX, Zhang YX and Gao LZ (2009) Combined U–Pb, hafnium and oxygen isotope analysis of zircons from meta-igneous rocks in the southern North China Craton reveal multiple events in the Late Mesozoic–Early Neoproterozoic. *Chemical Geology* **261**, 140–54.
- Lugmair GW and Marti K (1978) Lunar initial  $^{143}\text{Nd}/^{144}\text{Nd}$ : differential evolution of the lunar crust and mantle. *Earth and Planetary Science Letters* **39**, 349–57.
- Maniar PD and Piccoli PM (1989) Tectonic discrimination of granitoids. *Geological Society of America Bulletin* **101**, 635–43.
- Mao JW, Goldfarb RJ, Zhang ZW, Xu WY, Qiu YM and Deng J (2002) Gold deposits in the Xiaolinling–Xiong'er shan region, Qinling mountains, Central China. *Mineralium Deposita* **37**, 306–25.
- Mao JW, Pirajno F, Xiang JF, Gao JJ, Ye HS, Li YF and Guo BJ (2011) Mesozoic molybdenum deposits in the east Qinling–Dabie orogenic belt: characteristics and tectonic settings. *Ore Geology Reviews* **43**, 264–93.
- Mao JW, Xie GQ, Pirajno F, Ye HS, Wang YB, Li YF, Xiang JF and Zhao HJ (2010) Late Jurassic–Early Cretaceous granitoid magmatism in Eastern Qinling, central-eastern China: SHRIMP zircon U–Pb ages and tectonic implications. *Australian Journal of Earth Sciences* **57**, 51–78.
- Martin H, Smithies RH, Rapp R, Moyen JF and Champion D (2005) An overview of adakite, tonalite–trondhjemite–granodiorite (TTG), and sanukitoid: relationships and some implications for crustal evolution. *Lithos* **79**, 1–24.
- Middlemost EAK (1994) Naming materials in the magma/igneous rock system. *Earth Science Reviews* **37**, 215–24.

- Morel MLA, Nebel O, Nebel-Jacobsen YJ, Miller JS and Vroon PZ (2008) Hafnium isotope characterization of the GJ-1 zircon reference material by solution and laser-ablation MC-ICPMS. *Chemical Geology* **255**, 231–5.
- Naldrett AJ (1999) World-class Ni-Cu-PGE deposits: key factors in their genesis. *Mineralium Deposita* **34**, 227–40.
- Naldrett AJ (2004) *Magmatic Sulfide Deposits*. Heidelberg: Springer, 728 pp.
- Nasdala L, Hofmeister W, Norberg N, Mattinson JM, Corfu F, Dorr W, Kamo SL, Kennedy AK, Kronz A, Reiners PW, Frei D, Kosler J, Wan YS, Gotze J, Hager T, Kroner A and Valley, J (2008) Zircon M257 – a homogeneous natural reference material for the ion microprobe U–Pb analysis of zircon. *Geostandards and Geoanalytical Research* **32**, 247–65.
- Nebel O, Scherer EE and Mezger, K (2011) Evaluation of the  $^{87}\text{Rb}$  decay constant by age comparison against the U–Pb system. *Earth and Planetary Science Letters* **301**, 1–8.
- Nie ZR, Wang XX, Ke CH, Yang Y and Lv XQ (2015) Age, geochemistry and petrogenesis of Huashan granitoid pluton on the southern margin of the North China Block. *Geological Bulletin of China* **34**, 1502–16 (in Chinese with English abstract).
- Nyquist LE, Bansal B, Wiesmann H and Shih CY (1994) Neodymium, strontium and chromium isotopic studies of the LEW86010 and Angra dos Reis meteorites and the chronology of the angrite parent body. *Meteoritics* **29**, 872–95.
- Pearce JA (1996) Sources and settings of granitic rocks. *Episodes* **19**, 120–5.
- Peccerillo R and Taylor SR (1976) Geochemistry of eocene calc-alkaline volcanic rocks from the Kastamonu area, Northern Turkey. *Contributions to Mineralogy and Petrology* **58**, 63–81.
- Perugini D, Poli G, Christofides G and Eleftheriadis, G (2003) Magma mixing in the Sithonia Plutonic Complex, Greece: evidence from mafic microgranular enclaves. *Mineralogy and Petrology* **78**, 173–200.
- Petford N and Atherton M (1996) Na-rich partial melts from newly underplated basaltic crust: the Cordillera Blanca Batholith, Peru. *Journal of Petrology* **37**, 1491–521.
- Pirajno, F (2004) Hotspots and mantle plumes: global intraplate tectonics magmatism and ore deposits. *Mineralogy and Petrology* **82**, 183–216.
- Rapp RP, Shimizu N and Norman MD (2003) Growth of early continental crust by partial melting of eclogite. *Nature* **425**, 605–9.
- Rapp RP, Shimizu N, Norman MD and Applegate GS (1999) Reaction between slab-derived melts and peridotite in the mantle wedge: experimental constraints at 3.8 GPa. *Chemical Geology* **160**, 335–56.
- Rapp RP, Xiao L and Shimizu N (2002) Experimental constraints on the origin of potassium-rich adakite in east China. *Acta Petrologica Sinica* **18**, 293–311.
- Rasskazov SV, Brandt SB and Brandt IS (2010) *Radiogenic Isotopes in Geologic Processes*. Heidelberg: Springer, 306 pp.
- Ratschbacher L, Hacker BR, Calvert A, Webb LE, Crimmer JC, McWilliams MO, Ireland T, Dong S and Hu J (2003) Tectonics of the Qinling (Central China): tectonostratigraphy, geochronology, and deformation history. *Tectonophysics* **366**, 1–53.
- Salters VJM and Stracke A (2004) Composition of the depleted mantle. *Geochemistry, Geophysics, Geosystems* **5**, 1525–2027
- Sen C and Dunn T (1994) Dehydration melting of a basaltic composition amphibolite at 1.5 and 2.0 GPa: implications for the origin of adakites. *Contributions to Mineralogy and Petrology* **117**, 394–409.
- Skjerlie KP and Patino Douce AE (2002) The fluid-absent partial melting of a zoisite-bearing quartz eclogite from 1.0 to 3.2 GPa: implications for melting in thickened continental crust and for subduction-zone processes. *Journal of Petrology* **43**, 291–314.
- Sláma J, Košler J, Daniel JC., Crowley JL., Gerdes A, Hanchar JM., Horstwood MSA, Morris GA, Nasdala L, Norberg N, Schaltegger U, Schoene B, Tubrett MN and Whitehouse MJ (2008) Plešovice zircon: a new natural reference material for U–Pb and Hf isotopic microanalysis. *Chemical Geology* **249**, 1–35.
- Soderlund U, Patchett PJ, Vervoort JD and Isachsen CE (2004) The  $^{176}\text{Lu}$  decay constant determined by Lu–Hf and U–Pb isotope systematics of Precambrian mafic intrusions. *Earth and Planetary Science Letters* **219**, 311–24.
- Sun SS and McDonough WF (1989) Chemical and isotopic systematics of oceanic basalts: implications for mantle composition and processes. In *Magmatism in the Ocean Basins* (eds D Saunders and MJ Norry), pp. 313–45. Geological Society of London, Special Publication no. 42.
- Sun YS and Toksoz MN (2006) Crustal structure of China and surrounding regions from P wave traveltimes tomography. *Journal of Geophysical Research* **111**, B03310. doi: [10.1029/2005JB003962](https://doi.org/10.1029/2005JB003962).
- Tang GJ, Wang Q, Wyman DA, Chung SL, Chen HY and Zhao ZH (2017) Genesis of pristine adakitic magmas by lower crustal melting: a perspective from amphibole composition. *Journal of Geophysical Research: Solid Earth* **122**, 1934–48.
- Tang KF (2014) *Characteristics, genesis, and geodynamic setting of representative gold deposits in the Xiong'er shan district, southern margin of the North China Craton*. PhD thesis, China University of Geosciences, Wuhan, China. Published thesis (in Chinese with English abstract).
- Tang KF, Li JW, Selby D, Zhou MF, Bi SJ and Deng XD (2013) Geology, mineralization, and geochronology of the Qianhe gold deposit, Xiong'er shan area, southern North China Craton. *Mineralium Deposita* **48**, 729–47.
- Tang L, Zhang ST, Yang F, Santosh M, Li JJ, Kim SW, Hu XK, Zhao Y and Cao HW (2019) Triassic alkaline magmatism and mineralization in the Xiong'er shan area, East Qinling, China. *Geological Journal*, **54**, 143–156.
- Tian YF, Sun J, Ye HS, Mao JW, Wang XX, Bi MF and Xia XP (2017) Genesis of the Dianfang breccia-hosted gold deposit, western Henan Province, China: constraints from geology, geochronology and geochemistry. *Ore Geology Reviews* **91**, 963–80.
- Van der Meer QHA, Waight TE and Munker C (2017) Variable sources for Cretaceous to recent HIMU and HIMU-like intraplate magmatism in New Zealand. *Earth and Planetary Science Letters* **469**, 27–41.
- Van Der Meer QHA, Waight TE, Tulloch AJ, Whitehouse MJ and Anderen T (2018) Magmatic evolution during the Cretaceous transition from subduction to continental break-up of the Eastern Gondwana margin (New Zealand) documented by in-situ zircon O–Hf isotopes and bulk-rock Sr–Nd isotopes. *Journal of Petrology* **59**, 849–80.
- Vervoort JD, Patchett PJ, Albarede F, Blichert-Toft J, Rudnick R and Downes H (2000) Hf–Nd isotopic evolution of the lower crust. *Earth and Planetary Science Letters* **181**, 115–29.
- Vervoort JD, Patchett PJ, Söderlund U and Baker M (2004) Isotopic composition of Yb and the determination of Lu concentrations and Lu/Hf ratios by isotope dilution using MCICPMS: isotopic composition of Yb. *Geochemistry Geophysics Geosystems* **5**, Q11002. doi: [10.1029/2004GC000721](https://doi.org/10.1029/2004GC000721).
- Wang Q, Xu JF, Jian P, Bao ZW, Zhao ZH, Li CF, Xiong XL and Ma JL (2006) Petrogenesis of adakitic porphyries in an extensional tectonic setting, Dexing, south China: implications for the genesis of porphyry copper mineralization. *Journal of Petrology* **47**, 119–44.
- Wang Q, Xu JF, Zhao ZH, Bao ZW, Xu W and Xiong XL (2004) Cretaceous high-potassium intrusive rocks in the Yueshan–Hongzhen area of east China: adakites in an extensional tectonic regime within a continent. *Geochemical Journal* **38**, 417–34.
- Wang XL, Jiang SY and Dai BZ (2010) Melting of enriched Archean subcontinental lithospheric mantle: evidence from the ca. 1760 Ma volcanic rocks of the Xiong'er Group, southern margin of the North China Craton. *Precambrian Research* **182**, 204–16.
- Whalen JB, Currie KL and Chappell BW (1987) A-type granites: geochemical characteristics, discrimination and petrogenesis. *Contributions to Mineralogy and Petrology* **95**, 407–19.
- White WM (2013) *Geochemistry*. Oxford: Wiley-Blackwell, 668 pp.
- Windley BF, Maruyama S and Xiao WJ (2010) Delamination/thinning of subcontinental lithospheric mantle under Eastern China: the role of water and multiple subduction. *American Journal of Science* **310**, 1250–93.
- Wu FY, Yang YH, Xie LW, Yang JH and Xu P (2006) Hf isotopic compositions of the standard zircons and baddeleyites used in U–Pb geochronology. *Chemical Geology* **234**, 105–126.
- Xiao E, Hu J, Zhang ZZ, Dai BZ, Wang YF and Li HY (2012) Petrogeochemistry, zircon U–Pb dating and Lu–Hf isotopic compositions of the Haoping and Jinshanmiao granites from the Huashan complex batholith in eastern Qinling Orogen. *Acta Petrologica Sinica* **28**, 4031–46.
- Xie GQ, Mao JW, Li RL, Ye HS, Zhang YX, Wan YS, Li HM, Gao JJ and Zheng RF (2007) SHRIMP zircon U–Pb dating for volcanic rocks of the Daping Formation from Baofeng basin in eastern Qinling, China and its implications. *Acta Petrologica Sinica* **23**, 2387–96.

- Xu XS, Griffin WL, Ma X, O'Reilly SY, He ZY and Zhang CL** (2009) The Taihua group on the southern margin of the North China craton: further insights from U–Pb ages and Hf isotope compositions of zircons. *Mineralogy and Petrology* **97**, 43–59.
- Yao JM, Zhao TP, Li J, Sun YL, Yuan ZL, Chen W and Han J** (2009) Molybdenite Re–Os age and zircon U–Pb age and Hf isotope geochemistry of the Qiyugou gold system, Henan province. *Acta Petrologica Sinica* **25**, 374–84.
- Zhai L, Liu YG and Jiao YH** (2011) Geological features and ore-forming age of Miaoling gold deposit in Henan. *Jinlin Geology* **30**, 34–40 (in Chinese with English abstract).
- Zhang GW, Meng QG, Yu ZP, Sun Y, Zhou DW, Guo AL** (1996) Orogenesis and dynamics of the Qinling orogen. *Science in China Series D: Earth Sciences* **39**, 225–34.
- Zhao HX, Jiang SY, Frimmel HE, Dai BZ and Ma L** (2012) Geochemistry, geochronology and Sr–Nd–Hf isotopes of two Mesozoic granitoids in the Xiaoqinling gold district: implication for large-scale lithospheric thinning in the North China Craton. *Chemical Geology* **294–295**, 173–89.
- Zhao TP, Zhai MG, Xia B, Li HM, Zhang YX and Wan YS** (2004). Zircon U–Pb SHRIMP dating for the volcanic rocks of the Xiong'er Group: constraints on the initial formation age of the cover of the North China Craton. *Chinese Science Bulletin* **22**, 2342–9 (in Chinese with English abstract).
- Zheng JP, Sun M, Lu FX and Pearson N** (2003) Mesozoic lower crustal xenoliths and their significance in lithospheric evolution beneath the Sino-Korean Craton. *Tectonophysics* **361**, 37–60.